Meira Vinícius Tieppo (Orcid ID: 0000-0002-0947-9631)
Garcia-Casco Antonio (Orcid ID: 0000-0002-8814-402X)

Tectono-metamorphic evolution of the Central Ribeira Belt, Brazil: a case of late Neoproterozoic intracontinental orogeny and flow of partially molten deep crust during the assembly of West Gondwana

Vinícius T. Meira[1,2]*†, Antonio Garcia-Casco[3,4], Thaís Hyppolito[1,5], Caetano Juliani[6], Johann Hans D. Schorscher[7]

[1]Instituto de Geociências, Programa de Pós-Graduação em Geoquímica e Geotectônica, Universidade de São Paulo, São Paulo, Brazil

[2]Instituto de Astronomia, Geofísica e Ciências Atmosféricas, Departamento de Geofísica, Universidade de São Paulo, São Paulo, Brazil

[3]Facultad de Ciencias, Departamento de Mineralogía y Petrología, Universidad de Granada, Granada, Spain

[4]Instituto Andaluz de Ciencia de la Tierra, CSIC-Universidad de Granada, Armilla, Granada, Spain

[5]Facultad de Ciencias, Doctorado en Ciencias de la Tierra, Univesidad de Granada, Granada, Spain

[6]Instituto de Geociências, Departamento de Geologia Sedimentar e Ambiental, Universidade de São Paulo, São Paulo, Brazil

[7]Instituto de Geociências, Departamento de Mineralogia e Geotectônica, Universidade de São Paulo, São Paulo, Brazil

*Corresponding author: Vinícius Meira (vtmeira@unicamp.br)

†Currently at Instituto de Geociências, Departamento de Geologia e Recursos Naturais, Universidade Estadual de Campinas, Brazil

Key Points:

- We challenge the current tectonic model for the evolution of Central Ribeira Belt
- Based on structural, petrological and gechronological data we interpret the Central Riberia Belt as an intracontinental orogen
- A post-orogenic stage is characterized by widespread crustal melting related to wrench tectonics and flow of partially molten crust

This article has been accepted for publication and undergone full peer review but has not been through the copyediting, typesetting, pagination and proofreading process which may lead to differences between this version and the Version of Record. Please cite this article as doi: 10.1029/2018TC004959

Abstract

Recent advances in understanding the plate tectonics, intracontinental deformation and flow of partially molten crust have significantly improved our knowledge of collisional tectonics and the way in which we understand complex ancient orogens. The Central Ribeira Belt represents a Neoproterozoic fold-and-thrust belt formed in the Brasiliano Orogenic Cycle associated with the assembly of West Gondwana. This fold-and-thrust belt is currently interpreted as a result of recurrent collisions and amalgamation of terranes against large cratons. Based on an integrated structural, petrological and gechronological study in two metamorphic complexes of the Central Ribeira Belt (Embu and Costeiro complexes), we challenge the current model that involves multiple terrane collisions. Our data show for the first time metamorphic ages older than 600 Ma for samples from Costeiro and Embu complexes and suggest that both geological units experienced an intermediate-P metamorphism (M1) at circa 620 Ma and a low-P metamorphism (M2) at circa 575 Ma. Our proposed tectonic model is consistent with a M1 event related to an intracontinental orogeny, formed in response to the collision between the São Francisco Craton and the Parapanema Block. On the other hand, the later M2 metamorphism records extensional and wrench tectonics associated with orogenic collapse, constrained by the decompression paths of the metasedimentary sequences and M2-related S3 mylonitic foliation. The M2 metamorphism is associated with wide, right-lateral strike-slip shear zones and voluminous peraluminous magmatism in the Embu Domain and widespread partial melting of the middle crust forming migmatitic rocks and peraluminous leucogranites in the Costeiro Domain.

1 Introduction

Since the first formal proposals of the Plate Tectonics Theory by Wilson (1965), McKenzie and Parker (1967) and Morgan (1968), our understanding of geodynamics and its impact on the evolution of the Earth has steadily improved. Although these early workers assumed plate interior rigidity and narrowness of plate boundaries as central assumptions to constrain their mathematical models, the concept of diffuse plate boundaries and the evaluation of nonrigidity of plate interiors have emerged strongly over the last decades (see Gordon, 1998). Along with the concept of diffuse plate boundaries, ideas on intracontinental orogeny (e.g. Cunningham, 2005; Dyksterhuis & Muller, 2008; Neves et al., 2008), continental and oceanic core complexes (Whitney et al., 2013 and references therein) and crustal flow in compressive and extensional regimes (Beaumont et al., 2001; Vanderhaegue & Teyssier, 2001; Raimondo et al, 2009; McFadden et al., 2010b; Kruckenberg et al., 2011; among others) have recently been developed.

Although the early ideas of orogeny were focused on deformation along plate boundaries (e.g. Dewey & Bird, 1970; Sëngor, 1990), new findings on intracontinental tectonics provided a more realistic perspective of the evolving continental crust (e.g. Cunningham, 2005; Raimondo et al., 2014). Modern transpressional orogens in Central Asia (Cunningham, 2005), Tertiary intracontinental deformation in southeastern Australia (Dyksterhuis & Muller, 2008) and Ediacaran and Paleozoic intracontinental orogenies in central Australia (Shaw et al., 1991; Aitken et al., 2009; Raimondo et al., 2010) reveal the underappreciated importance of intracontinental deformation far from plate margins. Moreover, large-scale tectonic events such as growth and assembly of Gondwana and the Variscan and Alpine-Himalayan orogenies have produced significant crustal thickening at large distances from active plate margins (Vauchez et al., 1995; Ziegler et al., 1995; Tommasi & Vauchez, 1997; Matte, 2001; Neves, 2003; Rogers & Santosh, 2003; Cunningham, 2005, 2013; Aitken et al., 2013; Santosh et al., 2009; and references therein).

Exhumation processes associated with flow of partially molten crust also play an important role in global tectonics. In orogens and extensional settings, the flow of significant volumes of partially molten deep crust produces large-scale mobility of lower- and mid-crustal material (e.g. Vanderhaegue & Teyssier, 2001; Teyssier & Whitney, 2002; Rey et al., 2009a, Jamieson et al., 2011). Mid- to lower-crustal flow occurs frequently in tectonic settings dominated by compression (e.g. Beaumont et al., 2001, 2006; Raimondo et al., 2009). Likewise, migmatite-cored gneiss domes exposed within metamorphic core complexes commonly produce large-scale crustal flow (e.g. Tirel et al., 2004; Rey et al., 2009b, 2011; Kruckenberg et al., 2010). These gneiss domes record the P−T−t−d (pressure−temperature−time−deformation) evolution of both thickened crust under extension (e.g. Norlander et al., 2002; Whitney et al., 2003; Kruckenberg et al., 2011) and rift-related extensional settings (e.g. McFadden et al., 2010a, 2010b). Furthermore, these complexes and their hanging walls are frequently intruded by large volumes of granitic rocks (e.g. Catlos et al., 2012; Konstantinou et al., 2013) and migmatitic cores typically comprise a wide range in melt fractions, from metatexites to diatexites.

Based on these ideas, this paper re-evaluates the tectonic evolution of the Central Ribeira Belt (CRB) during the final configuration of West Gondwana during the Neoproterozoic. Traditionally, the CRB is interpreted as an orogenic belt formed by diachronous collision of several terranes or microplates (sensu Jones et al., 1983; Howell, 1989) during the closure of the Adamastor Ocean and the formation of Gondwana during the late Neoproterozoic Brasiliano Orogenic Cycle (e.g. Brito-Neves & Cordani, 1991; Campos Neto, 2000; Trouw et al., 2000). Here we offer a study that integrates new geological and structural mapping, thermobarometry and Sensitive High-Resolution Ion Microprobe (SHRIMP) dating of zircon of the CRB. Our aim is to constrain the architecture and tectonic evolution of this belt, and to evaluate the orogenic processes involved in the Neoproterozoic formation of West Gondwana, thereby adding new data to a recently proposed tectonic model for the Ribeira Belt (Meira et al., 2015). Particular attention is paid to the structure and P–T–t–d evolution of different structural domains (Embu and Costeiro domains) in order to address the roles of multiple terrane accretion versus intracontinental thickening of weakened lithosphere during supercontinental assembly.

2 Geological background

The Ribeira Belt constitutes the central part of the Mantiqueira Province (Almeida F.F.M. et al., 1981) and is characterized by a major NE–ENE-trending orogen-parallel strike-slip shear system, located in the Atlantic coast of the southeastern Brazil. It is bound by the Luis Alves Craton to the south, by the Southern Brasilia Belt and the Araçuaí Belt to the northwest and north, respectively. The northern limit corresponds to the inflexion of large-scale lineaments, roughly coincident with the transition from strike-slip- to thrust-dominated tectonic regimes (e.g. Vauchez et al., 1994; Egydio-Silva et al., 2005). The geological units of the Ribeira Belt include Paleoproterozoic crystalline inliers, Mesoproterozoic and Neoproterozoic metasedimentary sequences, voluminous Neoproterozoic granitic batholiths and small Ediacaran/Cambrian volcano-sedimentary basins (Campanha & Sadowski, 1999; Campos Neto, 2000; Janasi et al., 2001, 2009; Silva et al., 2005; Heilbron et al., 2008; Almeida R.P. et al., 2010, 2012; Siga Jr. et al., 2011; Vlach et al., 2011). All these units are variably reworked by the strike-slip shear system associated with the Neoproterozoic Brasiliano Orogenic Cycle.

Major NE-trending strike-slip shear zones delimit different geological domains, usually called “terranes”, within the Ribeira Belt (Fig. 1). The Central Ribeira Belt (CRB) comprises three geological domains separated by the Itu-Jundiuvira, Taxaquara-Rio Jaguari

and Lancinha-Cubatão shear zones (Figs. 1 and 2). The northwestern domain is called São Roque-Serra do Itaberaba Domain (SR-SI Domain) and its northwest limit with the Socorro-Guaxupé Domain (Southern Brasilia Belt) is delineated by the Itu-Jundiuvira Shear Zone. The SR-SI Domain consists of a Mesoproterozoic metavolcano-sedimentary sequence (Serra do Itaberaba Group), a Neoproterozoic siliciclastic-dominated low-grade metasedimentary unit (São Roque Group) and voluminous Ediacaran granitic batholiths (Juliani & Beljavskis, 1995; Juliani et al., 2000). To the southeast, the Taxaquara-Rio Jaguari Shear Zone separates the SR-SI Domain from the Embu Domain. The Embu Domain includes low- to high-grade metasedimentary rocks (Embu Complex), abundant syn-tectonic granitic bodies and stretched basement inliers reworked by the Brasiliano Orogeny (Fig. 2). The Costeiro Domain occurs along the Atlantic coast of the São Paulo and Rio de Janeiro states, and is separated from the Embu Domain by the Lancinha-Cubatão Shear Zone, and comprises essentially the Costeiro Complex and syn-tectonic granitoids (Fig. 2). The Costeiro Complex is comprised of high-grade metamorphic rocks, including migmatitic metapelites and metapsammites, calcsilicate rocks, boudins of amphibolites and orthogneisses. The syn-tectonic granitoids are Grt-bearing two mica leucogranites and Hbl-Bt-bearing granitoids.

3 Major structural features

The major structural pattern of the Central Ribeira Belt is characterized by orogen-parallel ENE-trending strike-slip shear zones (Fig. 2). However, the geometrical features and defomation pattern of the Central Ribeira Belt are different in both studied domains (Figs. 2 and 3). In the Embu Domain, the main foliation (S3) is associated with strike-slip shear zones and transposes an earlier foliation (S2). The earlier S2 foliation is recorded in low-strain zones between major strike-slip shear zones, usually delineating upright to inclined asymmetric open to tight folds with subhorizontal axis (Fig. 3). The main S3 foliation in the Costeiro Domain grades continuously from steeper to gently dipping orogen-parallel structures (Fig. 3), defined by the transposition of the earlier S2 foliation that is characterized by rootless intrafolial isoclinal folds.

3.1 Embu Domain

The regional S2 foliation is well preserved in the Embu Domain, mainly in low-strain zones between major strike-slip shear zones. It corresponds to a transposition foliation recorded, mainly in quartzites, by intrafolial isoclinal rootless F2 folds (Fig. 4a). Sigmoidal mafic boudins (Fig. 4b) and S/C structures suggest top-to-the SW sense of movement to the S2 foliation, however the kinematics associated with this deformational phase are still poorly constrained. In the higher-grade paragneisses, leucosomes and leucocratic veins occur parallel to the S2 foliation (Figs. 4a-b). The dispersion of the S2 poles is related to the cylindrical F3 fold pattern with built axes dipping S71°W/16° (Fig. 3a). The measured fold axis and built axes are subparallel to the mineral and stretching lineations (L3) that show an average orientation N69°E/6° (Figs. 3a-b).

The main S3 foliation constitutes a well-developed mylonitic foliation on major strike-slip shear zones, related to tight upright to steeply inclined folds (F3 folds), which transposes an earlier S2 foliation (Figs. 3c-d). The S3 foliation is orogen-parallel (~ENE–WSW) and has an average orientation of N68°E/81°NW (Figs. 3a-b). The F3 folds are asymmetric to upright with subhorizontal axis (Fig. 4c), subparallel to the orientation of the major strike-slip shear zones. Coeval emplacement of granitic bodies with predominantly peraluminous to slightly metaluminous compositions (Alves et al., 2013) constrains the D3 deformation to ca. 595–585 Ma (Alves et al., 2016; Meira, 2014). Magmatic foliation defines the S3 foliation in granitic apophysis (Fig. 4e), plutons and batholiths, usually associated with

orientation of aligned phenocrysts of feldspar and/or aggregates of micas (Alves et al., 2013; Meira, 2014). High temperature solid-state deformation is also observed, mainly at the edges of the granitic bodies (Fig. 4f). Dextral kinematics are inferred to the D3 deformational phase, suggested by macro-scale sigmoidal shape of the shear-related structures and granitic bodies (Figs. 1 and 2) and mesoscale S/C' fabrics and tension gashes in deformed porphyritic granites (Fig. 4f).

Microscopically, the relics of S2 foliation are observed as inclusion trails in garnet and staurolite porphyroblasts from mica schists, with the external S3 foliation defined by aligned micas and quartz ribbons (Fig. 4g). In the two mica granites, magmatic foliation appears in microstructures delineated by aligned muscovite and biotite grains and large euhedral feldspar crystals (Fig. 4h).

3.2. Costeiro Domain

The main foliation in the Costeiro Domain is represented by a pervasive to mylonitic S3 foliation in para- and ortho-derived gneisses that are variably migmatized (Fig. 5). A suprasolidus fabric characterizes the S3 foliation in the leucosomes, diatexites and peraluminous granites, although minor features of high temperature solid-state deformation are also observed. Both mylonitic/protomylonitic and suprasolidus S3 foliation are concordant and continuous from Embu Domain through to the Costeiro Domain, with steeper dips in the NW sector and gentle dips in the coastal sector of the Costeiro Domain (Figs. 2 and 3). Relics of the older S2 foliation are well preserved in rootless intrafolial isoclinal folds of metatexitic gneisses (Fig. 5a).

Two structural domains are identified within the Costeiro Domain: a sector with steeply dipping S3 foliation and average orientation of N60°E/72°NW, concentrated at the orthogneisses unit, Pico do Papagaio batholith and northwestern para-derived migmatitic rocks and amphibolite unit (Figs. 2 and 3c); and the sector with gently dipping S3 foliation with average orientation of N50°E/27°NW that comprises most of the para-derived migmatitic unit, the São Sebastião Leucogranite and the orthogneiss and metatexite unit (Figs. 2 and 3d). The mineral and stretching lineations associated with the main foliation (S3) are defined by biotite and sillimanite with general strike N–S to NE–SW and average orientation N13°E/18° (Figs. 2 and 3d).

Different kinematic indicators, including σ and δ -type porphyroclasts, S/C structures, inclined asymetric folds and sigmoidal schollen, suggest top-to-the S–SW sense of movement related to the development of S3/L3 structures (Fig. 5b). Discrete shear zones associated with intrusion of leucocratic veins deform the S3 foliation (Fig. 5c), and the sense of movement is compatible with that observed in the pair S3/L3. These structures may be related to late D3 deformation. Stromatic features in the metatexitic gneisses are parallel to the S3 foliation and the leucosomes show both suprasolidus and high temperature solid-state deformation patterns (Fig. 5d). Diatexites and the peraluminous São Sebastião Granite (Fig. 2) show mostly magmatic flow structures delineated by pervasive orientation of feldspar crystals and mica aggregates (e.g. biotite schlieren) (Figs. 5e–f), however high temperature solid-state deformation also occurs. Crystallization ages of diatexites and peraluminous São Sebastião Granite (Meira, 2014) indicate that the D3 deformational phase continued until at least 570–560 Ma.

At the microscopic scale, relics of S2 foliation are recorded by rootless isoclinal microfolds defined by aligned biotite, sillimanite and quartz/feldspathic bands (Fig. 5g).

4 Metamorphic petrology and thermobarometry

Mineral compositions were determined by wavelength-dispersive spectrometry (WDS) with a Cameca SX-100 microprobe (CIC-University of Granada), operated at 15–20 kV and 15 nA beam current. Plotting of the minerals in ternary ACF and AFM compatibility diagrams was done using CSpace software (Torres-Roldán et al., 2000). Elemental X-ray maps were obtained with the same Cameca SX-100 microprobe operated at 20 kV and 200-300 nA beam current with step size (pixel) of 8 μm and counting time of 45 ms. The processing of the images was performed with DWImager software developed by R. Torres-Roldán and A. Garcia-Casco (see Garcia-Casco, 2007 for quantification of the images).

Representative samples from the Costeiro and Embu complexes were selected for description metamorphic petrology and thermobarometric calculations, including the metasedimentary sequences and associated amphibolitic rocks. Detailed descriptions of the samples, including textures, mineral assemblages and mineral chemistry are available in the Supporting Information (Supporting Information S1, Table S1, Figure S1, Figure S2 and Figure S3).

4.1 P−T conditions and paths

Pressure and temperature were estimated from isochemical phase diagrams calculated with THERIAK-DOMINO software, version 04.02.2017 (de Capitani & Brown, 1987; de Capitani & Petrakakis, 2010) and the optimal multi-equilibrium average P−T method of Powell and Holland (1994) with THERMOCALC software (Holland & Powell (1998); version 3.33, dataset tc-ds55, 26 October 2009). The isochemical phase diagrams calculations were performed in the system MnNCKFMASHT (Mn was excluded from calculations of sample with less than 0.10 wt% of Mn) using the internally consistent thermodynamic dataset of Holland and Powell (1998; update 5.5, tcds55_p07; available in http://dtinkham.net/peq.html) and the solution models of Holland and Powell (1998) for staurolite, chloritoid, chlorite, cordierite and epidote; Holland and Powell (2003) for feldspar (plagioclase and K-feldspar; PLC1); Coggon and Holland (2002) for white mica (WM02V); White et al. (2000) for ilmenite (ILM0); White et al. (2002) for spinel and orthopyroxene; White et al. (2005) for garnet and biotite (in Mn systems); White et al. (2007) for garnet and biotite (GT07W2 and BI07, respectively, in systems without Mn), and silicate melt. A correction of CaO allocated to apatite was done by subtracting an amount of CaO from the total using the bulk P_2O_5 concentration as a proxy of apatite. Ferric iron was excluded. The calculations were performed assuming water saturation at subsolidus conditions for samples from Embu Complex. The amount of water component at supersolidus conditions was estimated from the intersection of solidus and H_2O-saturated curves in T-XH_2O equilibrium diagram (Figure S9). The optimal average P−T estimates include calculations using different phase assemblages grown at near-peak and post-peak metamorphic conditions, assuming H_2O-fluid in all assemblages. Recalculation of the chemical mineral analyses, including ferric iron estimates, activity of each end-member and its uncertainty (1σ), were achieved using AX software (downloadable from www.esc.cam.ac.uk/research/research-groups/holland/ax). The optimal average P−T calculations and data treatment followed the method described in Powell and Holland (1994). The results of these estimations are presented in Table 1.

4.1.1 Embu Complex

A metasedimentary sample and a mylonitic metagranite were modeled to constrain the metamorphic evolution of the Embu Complex. The metasedimentary rock (PSM-111B) is a mylonitic staurolite-garnet-bearing mica schist (Fig. 6a) and the mylonitic metagranite (PSM-75C) is a fine-grained, garnet-bearing mica-rich mylonite (Fig. 6b). AFM diagrams are

presented with near-peak assemblages for both samples (Fig. 6c). The mineral abundance (visual estimates) of the studied samples is shown in Table 2.

P−T estimates were calculated for both samples (PSM-111B; PSM-75C). Due to the high degree of retrogression in the matrix associated with late mylonitization (see Supporting Information for details), near-peak conditions were constrained essentially by the calculated stability field of the mineral assemblages and the distribution of compositional isopleths of garnet, staurolite and plagioclase porphyroblasts in isochemical phase diagrams, because these phases better retain peak compositions due to sluggish volume-diffusion kinetics in comparison with phyllosilicates, for example. The retrograde conditions were calculated using the multi-equilibrium average P−T method on reequilibrated/newly formed phases.

For the staurolite-garnet-bearing mica schist (PSM-111B), the peak assemblage St+Grt+Ms+Bt±Rt+Qz+H_2O (abbreviations of Whitney and Evans (2010)) is constrained at conditions between 7.0−~13.0 kbar and 570−640 °C. These conditions are further constrained by the measured near-peak Mg# of staurolite (0.15±0.01) and X_{Alm} of garnet (0.79±0.01) and indicate near-peak conditions between 8.6–9.75 kbar and 610–640 °C (Fig. 7). Although Ti oxides have not been described as inclusions within garnet and staurolite porphyroblasts, the calculations predicted only trace amounts of rutile (less than 0.5 %) in near-peak conditions. Multi-equilibrium estimates yield near-peak conditions around 9.0 kbar and 600 °C, with associated errors (Table 1; Fig. 8a) in agreement with the isochemical phase diagram estimations. Retrograde rims re-equilibrated during cooling occur in both garnet and staurolite porphyroblasts; nevertheless, this retrograde zonation is absent in the contact zone between them (Fig. 9). The calculations of retrograde conditions for the assemblage Grt (outermost rim)+matrix Ms and Bt+Chl+Pl(rim)+Ilm+Qz+H_2O yielded circa 4.0 kbar and 560 °C (Fig. 8a).

The near-peak conditions of the garnet-bearing mica-rich mylonite (PSM-75C) are constrained by the stability field of the assemblage Grt+Ms+Bt+Pl+Ilm+Qz+H_2O in isochemical phase diagram, yielding a large P–T field with conditions of up to 8.8 kbar and between 525−670 °C (Fig. 10). The intersection of X_{Alm} isopleths for the near-peak garnet composition (X_{Alm}=0.73±0.01) and X_{An} of near-peak plagioclase (X_{An}=0.24−0.25±0.01) yields P−T conditions between 7.5–8.25 kbar and 620–655 °C (Fig. 10). The retrograde condition was estimated by the multi-equilibrium average P−T method with Grt (lower X_{prp} and higher X_{sps} outermost rim)+matrix Ms and Bt+Pl+Chl+Ilm+Qz+H_2O and yielded circa 3.0 kbar and 530 °C (Table 1; Fig. 8a).

The estimated P−T path for the Embu Complex based on these two samples involves near-isothermal decompression from 7.0–9.0 to ~3.0 kbar at temperatures around 610−650 °C.

4.1.2 Costeiro Complex

Amphibolitic and metasedimentary rocks were selected for assessing the metamorphic conditions of the Costeiro Complex. The amphibolitic rocks comprise medium- to fine-grained amphibolites, including medium-grained garnet-bearing amphibolites and clinopyroxene-bearing amphibolites (Figs. 11a−c). The ACF diagram shows the distribution of the cofacial amphibolitic rocks, with different mineral assemblages being controlled by the bulk composition of the samples (Fig. 11d). Note that “ordinary” amphibolites plot on the tieline amphibole–plagioclase, as expected. Two major groups of metasedimentary rocks were targeted for petrological studies: sillimanite-bearing garnet-biotite paragneisses (metapelites) (Figs. 12a and b) and metagreywacke rocks including amphibole-bearing garnet-biotite paragneisses (Figs. 12c and d). Geochemical data from these groups plot above

and below the garnet−biotite tieline, respectively, in the AFM diagram (Fig. 12e). The mineral abundances (visual estimates) of the studied samples are shown in the Table 2.

Four metasedimentary (PSM-60B, PSM-104A1, PSM-104D, PSM-109E) and four amphibolitic (PSM-61A, PSM-61B, PSM-106A, PSM-106D) samples were used to constrain the P−T conditions of the Costeiro Complex. One isochemical phase diagram was calculated for metasedimentary sample PSM-104A1 in order to estimate near-peak P–T conditions. Multi-equilibrum average P−T calculations were performed for near-peak and retrograde conditions in both metasedimentary and amphibolitic rocks.

The near-peak assemblage of Grt+Sil+Bt+Kfs+Pl+Ilm+Qz+L (L=silicate liquid) of the metapelitic group (Sil-bearing Grt-Bt paragneiss – PSM-104A1) is modeled in the isochemical phase diagram by a penta-variant field at $4.2<P<6.8$ kbar and $690<T<775$ °C (Fig. 13). The intersection of X_{Alm} isopleths for the near-peak garnet composition ($X_{Alm}=0.70\pm0.01$) and X_{An} isopleths for near-peak plagioclase provide near-peak P−T conditions of 5.0–6.8 kbar and 715–760 °C (Fig. 13). The multi-equilibrium average P−T calculations for the sillimanite-bearing garnet-biotite paragneiss samples PSM-104A1, PSM-104D and PSM-109E using the phases Grt±Sil+Bt±Ms+Pl+Qz+H_2O yield near-peak conditions of 3.5−7.0 kbar and 600−750 °C (Table 1; Fig. 8b), in agreement within error with the isochemical phase diagram estimation. The near-peak average P−T estimates for the metagreywacke group (Amp-bearing Grt-Bt paragneiss – PSM-60B) yield conditions of circa 3.5 kbar and 650 °C (Table 1; Fig. 8b). Moreover, the Grt-bearing amphibolites provided near-peak estimates of circa 650−750 °C and 4.5−5.5 kbar (Table 1; Fig. 8b). The near-peak conditions calculated for the amphibolites plot beyond the H_2O-saturated basaltic solidus. Hence, if fluid locally fluxed the amphibolites they may have evolved (small) fractions of partial melts. The calculated retrograde conditions yielded circa of 530 °C and 4.5 kbar (Table 1; Fig. 8b).

5 Zircon geochronology

Zircon separation techniques followed the conventional magnetic and density techniques. Zircon grains were handpicked, mounted, polished and imaged by cathodoluminescence (CL) and optical microscope at the IBERSIMS laboratory of the University of Granada. Analytical sites were selected based on internal zonation and complexity, and morphological features of the grains. A wide range of morphology and internal textures were analyzed for U−Pb, including inherited cores, primary magmatic concentric oscillatory zoning and metamorphic overgrowths. The U−Pb analyses were obtained using a SHRIMP IIe/mc ion microprobe at the IBERSIMS laboratory of the University of Granada. The SHRIMP analytical method is available in www.ugr.es/~ibersims. The calibration of uranium concentration was achieved using the SL13 reference zircon (U: 238 ppm). U−Pb ratios were calibrated using the TEMORA-1 reference zircon (417 Ma) (Black et al., 2003) which was measured every 4 unknowns. Point-to-point errors (95% confidence interval) on the age standard were ±0.23% for $^{206}Pb/^{238}U$ and ±0.46% for $^{207}Pb/^{206}Pb$. Data reduction was performed with the SHRIMPTOOLS software (downloadable from www.ugr.es/~fbea) using the STATA™ programming language.

U−Pb zircon dating was collected from representative samples of metasedimentary rocks from both complexes and an amphibolitic rock from Costeiro Domain. The zircon rim analyses on metamorphic overgrowths were performed in order to date the medium- to high-grade metamorphism of both complexes. The descriptions of the dated samples are presented in the Supporting Information (Text S2).

The spatial distribution of the samples is shown in the Figure 2. All analytical data and CL images from all analyzed grains are presented in the Supporting Information (Table S2 and Figures S10 and S11). All errors and weighted mean ages are quoted at 95% confidence level (2σ). Age uncertainties lower than 1% are unreliable considering analytical limitations and it must be treated as statistical artifacts. Age data for all zircon samples were plotted on Wetherill diagrams (Figs. 14 and 15) using SHRIMPTOOLS software. The weighted mean ages were calculated using IsoplotR software (Vermeesch, 2018). The $^{206}Pb/^{238}U$ ages were chosen as effective ages.

Metamorphic overgrowths were analyzed on zircon grains from impure quartzites of the Embu Complex (PSM-88B; PSM-96; PSM-98A) and metatexitic paragneisses (PSM-51E; PSM-60F; PSM-61J; PSM-108C; PSM-109A) and a garnet-bearing amphibolite (PSM-104G) of the Costeiro Complex. In general the metamorphic overgrowths constitute homogeneous dark or bright luminescent rims (Figures S10 and S11). Homogeneous and slightly zoned bright luminescent grains also occur. Dissolution and recrystallization textures are present in the interface between the detrital cores and the metamorphic overgrowths (Figures S10 and S11).

The zircon grains from the impure quartzites of the Embu Complex are between 100 and 200 μm and comprise detrital cores with oscillatory growth zoning mantled by dark luminescent homogeneous rims (Figure S10). The analyses on these dark luminescent homogeneous rims yielded mean weighted $^{206}Pb/^{238}U$ ages around 575 Ma (575±2 Ma, MSWD=9.00 – PSM-88) and 610-620 Ma (613±3 Ma, MSWD=6.44 –PSM-98A; spot ages of 605±4 and 618±7 Ma – PSM-96) (Fig. 14). Two groups of ages, based only on spot ages, can be defined in zircon overgrowths from sample PSM-98A (620±4 Ma, MSWD=0.64 and 607±4 Ma, MSWD=2.76; Fig. 14), although these groups are constrained by only a few analyses (Fig. 14). The low Th/U ratio of these analyses (lower than 0.25) (Fig. 16a) supports the metamorphic origin for the homogeneous rims (e.g. Rubatto, 2002). High values of reduced chi-squared (MSWD) suggest over dispersion of data or underestimation of the age uncertainties (Spencer et al., 2016).

In the metatexitic paragneisses from the Costeiro Complex, the zircon grains include detrital cores mantled by homogeneous rims and homogeneous to slightly zoned grains (Figure S11). The zircon grains from samples PSM-51E, PSM-61J and PSM-109A are around 100 μm-long and contain bright to gray luminescent homogeneous rims. The analyses of these homogeneous rims provided scattered ages around 560 and 635 Ma (PSM-51), a poorly-constrained mean weighted $^{206}Pb/^{238}U$ age of circa 620 Ma (619±2 Ma, MSWD=21.40 – PSM-61J) and a mean weighted $^{206}Pb/^{238}U$ age of 618±3 Ma, MSWD=2.95 (PSM-109A) (Fig. 15). The zircon grains from samples PSM-60F and PSM-108C comprehend bright luminescent homogeneous to slightly zoned grains and rims (Figure S11). The analyses from both samples, including the homogeneous grains and overgrowth rims, yielded mean weighted $^{206}Pb/^{238}U$ ages around 625 Ma (626±2 Ma, MSWD=6.07 and 626±3 Ma, MSWD=12.30 – respectively, PSM-60F and PSM-108C) (Fig. 15). Based on spot ages, an older age at around 640 Ma can be distinguished in a group of 4 analyses from sample PSM-60F (640±5 Ma, MSWD=0.72; Fig. 15). Textural features and the low Th/U ratio of the overgrowth rims from the samples PSM-51E, PSM-61J and PSM-109A suggest a metamorphic origin for these overgrowths (Fig. 16a) (e.g. Rubatto, 2002; Corfu et al., 2003; Hoskin and Schaltegger, 2003). On the contrary, the analyses of the homogeneous grains and overgrown rims from samples PSM-60F and PSM-108C yielded high Th/U ratios (Fig. 16a), even though the textural features suggest a metamorphic origin. The high Th/U ratios might be related to the greywacke composition of these amphibole-bearing garnet-biotite paragneisses (see Text S2 for details) and/or zircon growth or re-equilibration involving a

melt phase (Schaltegger et al., 1999). Over dispersion of the data or underestimation of the age uncertainties must be considered for weighted mean ages with high MSWD values (Spencer et al., 2016).

The zircon grains from sample PSM-104G (garnet-bearing amphibolite) are characterized by prismatic to ovoid crystals, varying in size from 40 up to 120 μm-long (Figure S11). Internal textures comprise oscillatory growth and convolute zoning cores with homogeneous gray to dark luminescent overgrowth rims and homogeneous bright luminescent grains (Figure S11). Homogeneous grains, cores with convolute zoning, and overgrowth rims yielded two well-defined groups of ages at around 580 and 615Ma (583±5 Ma, MSWD=2.11 and 614±2 Ma, MSWD=3.96; Fig. 15). The age groupings were separated based only on spot ages. The values of reduced chi-squared (MSWD) around 2.0 and 4.0 might indicate underestimated age uncertainties. Low Th/U ratios and textural features (lower than 0.05) (Fig. 16a) support the metamorphic origin for those analyzed grains and overgrowth rims.

6 Discussion

6.1 Timing of metamorphism and the late Neoproterozoic tectonic evolution of the Central Ribeira Belt (CRB)

The current tectonic models for CRB assume recurrent collision and accretion of different terranes, including the Embu and Costeiro domains, after 600 Ma (e.g. Campos Neto & Figueiredo, 1995; Campos Neto, 2000; Heilbron et al., 2004; Silva et al., 2005). However, our data show for the first time evidences of an older metamorphic overgrowth stage (M1) of around 620 Ma in zircon grains from both Embu and Costeiro domains. Scattered U-Pb ages suggest episodic growth of zircon at any time within 640-610 Ma range in both domains. Indeed, this ~30 Myr lasting metamorphic event is also recorded on collisional-related high-grade metamorphic rocks in the Southern Brasilia Belt (Reno et al., 2012; Tedeschi et al., 2017, 2018; Rocha et al., 2018) (Figs. 16c and d). The younger metamorphic overgrowth stage (M2 − ~570-580 Ma) identified in zircon grains from both domains is coeval with the crystallization of migmatitic diatexites, anatectic peraluminous leucogranites (Meira, 2014) and A-type alkali-calcic porphyritic granites in the Costeiro Domain (Meira et al., 2014; Meira, 2014), and voluminous peraluminous magmatism in the Embu Domain (Alves et al., 2013; Meira, 2014) (Fig. 16e). The spread of metamorphic ages presented in this work is also seen in ages of magmatic zircons (Alves et al., 2013; Meira, 2014) and may indicate prolonged high-temperature and melt-bearing conditions (at least 10-20 Myr) in the middle crust during the post-collisional stage.

In our tectono-metamorphic model for the Central Ribeira Belt, the older metamorphism (M1) is interpreted as an intracontinental orogeny in a hinterland setting associated with the far-field stress propagation from the collision between the Parapanema Block and the São Francisco Craton. This intracontinental deformation inverted the Neoproterozoic basins in all domains of the Central Ribeira Belt, forming the S1 and S2 foliations in the Embu and Costeiro domains. In the latter, only the M1-related S2 foliation is preserved as intrafolial isoclinal folds. M1 metamorphism reached intermediate pressure and temperature (~8.0 kbar, 600 °C) in the Embu Domain (Fig. 16b), even though M1-related migmatites also occur in this domain (Fig. 4a) suggesting higher temperature regimes. Evidence of the intermediate pressure M1 metamorphism in the Costeiro Domain has not been found, possibly due to the high temperature M2 overprint (~650−750 °C and ~4.0−6.0 kbar; Fig. 16b) that affected this domain. However, kyanite- and staurolite-bearing mica schists of the Turvo-Cajati Formation, possibly structurally correlated with the Costeiro

Domain in the south, record intermediate pressure collision-related metamorphism (Faleiros et al., 2011). Low-pressure M2 metamorphism is associated with widespread crustal melting, including voluminous peraluminous magmatism in the Embu Domain and migmatization in the Costeiro Domain, and also with the development of migmatite-cored gneiss domes and wide right-lateral strike-slip shear zones. The associated S3 foliation is a M2-related fabric and is characterized by a steep mylonitic foliation in the Embu Domain and moderately dipping domed mylonitic foliation in the Costeiro Domain. The kinematic indicators for the strike-slip shear zones are in agreement with regional dextral escape tectonics (previously interpreted as an oblique collisional regime) (Faleiros et al., 2011). However the top-to-the-S–SSW sense of movement for the low- to intermediate-angle shear zones of the Costeiro Domain does not fit in a simple regional tectonic-related stress field (e.g. dextral positive flower structure of Campanha and Ens (1996)). We suggest that the lower-angle shear zones of the São Sebastião region could be associated with crustal flow of the molten middle crust, as migmatite-cored gneiss domes (Fig. 16e) in the sense of Teyssier and Whitney (2002) and Rey et al. (2011). In this context, the strain-field in this region might be controlled by gravity in a topographic overload scenario, similar to what was suggested by Mondou et al. (2012) for the Araçuaí Belt. Furthermore, our model is in agreement with models of intracontinental deformation (e.g. Neves, 2003; Raimondo et al., 2014; and references therein) and crustal flow in extensional regimes (Vanderhaegue & Teyssier, 2001; McFadden et al., 2010b; Kruckenberg et al., 2011; among others), and allow the consideration of domain/terrane tectonics in the Ribeira Belt in the context of diffuse plate boundary models (e.g. Gordon, 1998) rather than rigid plate models of several subduction and collisional processes.

6.2 Conflicting tectonic models for the late Neoproterozoic

Diachronous collision of small continental masses (terranes or microplates) against large cratons is largely considered the main process of the Brasiliano Orogeny and West Gondwana formation (e.g. Brito Neves & Cordani, 1991; Brito Neves et al., 1999; Silva et al., 2005). Although oceanic closure associated with subduction and collision played an important role in the Brasiliano Orogeny (e.g. Campos Neto & Caby, 2000; Lenz et al., 2011; Ganade de Araujo et al., 2014), the evolution of the Central and Northern Mantiqueira Province is still debated (e.g. Almeida R.P. et al., 2010; Mondou et al., 2012). The alternative tectonic model presented here for the formation of the Ribeira Belt considers a much simpler puzzle of tectonic plates with subduction of an oceanic crust beneath the Paranapanema Block and consequent collision with the passive margin of the São Francisco Craton (Fig. 16). In this model, the basins of the Ribeira and Araçuaí belts were developed in an intracontinental environment and were inverted as a consequence of this event.

First-order inconsistencies in the model of recurrent microplate collisions in the Ribeira Belt and the closure of an ocean in the Araçuaí Belt include: a) the non-agreement, in a broader sense, between the geological records of upper crustal (e.g. Ediacaran−early Cambrian rift-related basins) and middle-lower levels (e.g. terrane collisions and accretion) (e.g. Almeida R.P. et al., 2010, 2012; Heilbron et al., 2013), and b) the restricted size of the hypothetic Adamastor Ocean (e.g. Pedrosa-Soares et al., 2001; Alkmim et al., 2006) to accommodate several drifting small continental plates (see Fossen et al., 2017). Another critical issue involves the interpretation of Neoproterozoic tonalitic to granodioritic batholiths in the Ribeira and Araçuaí belts as magmatic arcs (e.g. Heilbron et al., 2013; Pedrosa-Soares et al., 2001, 2011). Recent detailed structural and geochronological studies of the Central Plutonic Unit of the Araçuaí Belt showed that the emplacement of the tonalitic magmas occurred around 580 Ma, contemporaneous with regional metamorphism (Mondou et al., 2012). The similarity of the magmatic to sub-magmatic fabric of the tonalites and the solid-state fabric of the host rocks, the lack of solid-state deformation in the tonalites and the

coeval regional deformation, tonalitic magma emplacement and partial melting of middle crust altogether contradict the previously suggested subduction-related magmatism (pre-collisional magmatism G1 of Pedrosa-Soares et al. (2001)) of the two main tonalitic (Galiléia and São Vitor) batholiths in the Araçuaí Belt (Mondou et al., 2012 and references therein). Moreover, detailed structural studies indicate a complex 3D deformation flow pattern associated with spatial variations in strain-field due to a combination of far-field tectonic and gravitational forces (Mondou et al., 2012; Cavalcante et al., 2013).

The previously suggested multiple terranes collage model for the Ribeira Belt considered the time span of 560−530 Ma (Campos Neto and Figueiredo, 1996) and 600−550 Ma (Heilbron and Machado, 2003) for the collision of Serra do Mar (or Oriental) Terrane (here called the Costeiro Domain) against the already accreted Embu (or Ocidental) Terrane (here called the Embu Domain). If our data, including intermediate-P M1 metamorphism at ~620 Ma and low-P M2 metamorphism at ~575 Ma coeval with calc-alkaline porphyritic granites in the Costeiro Domain (Meira, 2014; Meira et al., 2014) and voluminous peraluminous magmatism in the Embu Domain (Alves et al., 2013; Meira, 2014), were interpreted in terms of the recurrent terrane/microplate accretion model they would require the timing of terrane accretion to be extended to ~ 640-620 Ma and the establishment of a new subduction zone at the rear (east) of the accreted terrane in order to create a magmatic arc. This odd tectonic history contrasts with our much simpler intracontinental model for the tectonic evolution of these fold belts.

6.3 Tectonic subdivision of the Central Ribeira Belt and some insights on paleogeographic reconstructions

Since the works of Hasui and Sadowski (1976), the Precambrian rocks of the southeastern Brazil, including the Central Ribeira Belt and the Southern Brasilia Belt, are subdivided in four different geological blocks delimited by major strike-slip shear zones (Socorro–Guaxupé Domain; São Roque–Serra do Itaberaba Domain; Paranapiacaba or Embu Domain; and Costeiro Domain). Although this initial proposal of division was for purposes of description, later propositions contained large interpretative conceptions (e.g. Campos Neto, 2000; Heilbron et al., 2004, 2008). The division in vogue considers the different domains as "tectono-metamorphic" terranes and their limits as suture zones (e.g. Heilbron et al., 2008; Faleiros et al., 2011; Tupinambá et al., 2012). Nevertheless, new geochronological and petrological data has challenged the *status quo* of this interpretative division (Almeida R.P. et al., 2010; Trouw et al., 2013; Meira, 2014; Meira et al., 2015, and this study).

Based on detailed geological mapping, structural analysis and geochronological data, Trouw et al. (2013) argued that the separation of the Embu and the Socorro–Guaxupé domains as two distinct tectonic units should be abandoned and interpreted the Embu Domain as the southward continuation of the Southern Brasilia Belt (called by these authors Brasilia/Ribeira interference zone). Furthermore, the new petrological and geochronological data, including P−T−t−d paths, metamorphic overgrowths in zircon grains, timing of migmatization and crystallization of granitoids, together with lack of oceanic remants and high-P metamorphism between the studied domains, suggest that the Embu and Costeiro domains were part of a single lithospheric plate since at least ~650 Ma. Hence, a phase of intracontinental orogeny is proposed for the intermediate-P M1 metamorphism recorded in both domains (Fig. 16d), followed by a phase of wrench tectonics associated with gneiss dome development and low-P high-temperature M2 metamorphism (Fig. 16e). Considering the above-mentioned arguments, the division of the Embu and Costeiro domains into distinct tectonic terranes (or microplates) should be avoided, at least for the final stages of the assembly of Western Gondwana. A new limit between these two geological domains is

proposed in this study (see discussion in Meira, 2014) and this division should be used for descriptive purposes only, circumventing interpretative misconceptions. In this context, the metasedimentary sequences of the whole Central Ribeira Belt should be considered as part of the eastern Parapanema Block (Fig. 16) and the deposition of these metasedimentary sequences should be associated with different basin stages, including Mesoproterozoic (e.g. Serra do Itaberaba Group and Embu Complex?) and Neoproterozoic (e.g. São Roque Group, Costeiro Complex and Embu Complex?) sedimentary successions. Both Embu and Costeiro domains might represent the hinterland of the Southern Brasilia Belt, connected northward to a *stricto sensu* intracontinental setting (Araçuaí Belt) between São Francisco and Congo cratons (Meira et al., 2015; Fossen et al., 2017).

Accordingly to our tectonic evolutionary model, a more than 1500 km-long continuous rift system, active along the southeastern South America during the middle Ediacaran−early Cambrian, indicates an important extensional event in the Mantiqueira Province (Almeida R.P. et al., 2010, 2012). Small fault-bounded siliciclastic and volcaniclastic basins and voluminous coeval granitic magmatism characterize this rift system and imply that all the terranes involved in the collisional stages of the Brasiliano Orogeny in the Mantiqueira Province were united in a single plate already at ~650−600 Ma (Almeida R.P. et al., 2010; this work). Hence, the model of diachronous collision of different terranes proposed by many authors (e.g. Brito Neves et al., 1999; Heilbron et al., 2004; Silva et al., 2005) for the Ediacaran to early Cambrian periods in the Central Ribeira Belt must be re-evaluated.

7 Conclusions

In this paper we present new data that corroborate with a recently proposed tectonic model for the evolution of the Central Ribeira Belt (Meira et al., 2015) during the late Neoproterozoic (Fig. 16). Taking into consideration new advances in the understanding of orogenic belts, including intracontinental deformation and flow of partially molten crust, we propose that the whole Central Ribeira Belt evolved as a weakened crustal sector that was thickened in an intracontinental environment at circa 620 Ma (M1 metamorphism) followed by recurrent extensional and wrench tectonics at around 575 Ma (M2 metamorphism). We conclude that the Embu and Costeiro domains were already assembled by 650 Ma, and perhaps as early as at ca. 790 Ma when intracontinental basaltic and granitic magmatism intruded the Costeiro and Embu domains (Meira, 2014).

The older M1 metamorphism indicates burial of the metasedimentary successions up to 8.0 kbar (down to ~25 km depth), reaching amphibolite facies conditions. A contractional regime with crustal thickening produced two foliations (S1 and S2), usually recorded by rootless isoclinal intrafolial microfolds. Near-isothermal decompression down to ~3.0 kbar (~10 km depth) at temperatures of ~550−600 °C characterizes the younger M2 metamorphism in the Embu Domain. Wide right-lateral strike-slip shear zones typify the D3 deformation phase (S3 mylonitic foliation) during the ensuing cooling and decompression stage. In the Costeiro Domain, however, M2 metamorphism involved heating with moderate decompression and peak conditions of ~650−750 °C and ~4.0−6.0 kbar (ca. 12–18 km depth), followed by cooling and decompression. Heating to upper amphibolite conditions reached by the rocks of Costeiro Domain caused widespread partial melting of the middle crust during decompression, forming migmatitic rocks and peraluminous leucogranites. The low angle deformation fabric (S3 mylonitic foliation) associated with this metamorphic phase is interpreted as extensional crustal flow of middle molten crust.

Our new data and interpretations of tectonic evolution of the Ribeira Belt are in agreement with the chronologic and structural evolution of Ediacaran-early Cambrian rift-related basins and of the tonalitic batholiths of the Araçuaí Belt. Furthermore, the Tonian magmatism and metamorphism in both Costeiro and Embu domains suggests a much longer shared tectonic history for these geological domains, arguing against the multiple terrane accretion hypotheses for the tectonic evolution of the Ribeira belt. Nevertheless, detailed petrochronological data are necessary to test the new proposed tectonic model and contribute to the better understanding of the Ribeira Belt tectonic evolution.

Acknowledgments, Samples, and Data

The first author is thankful to CAPES and CNPq for the PhD scholarships and CAPES for post-doctoral fellowship. T. Hyppolito acknowledges São Paulo Research Foundation for a post-doctoral fellowship (FAPESP Grant, #2014/23422-0). Fernando Bea and Pilar Montero are thanked for their help with SHRIMP analysis and data treatment. Lucas Schiavetti and Glaucia Barreto are thanked for field assistance. Haakon Fossen is fully acknowledged for his comments and suggestions on the first version of this manuscript. Aitor Cambeses is acknowledged for fruitful discussions and help with the illustrations. Thanks are due to the COTEC-IF and workers of the Parque Estadual da Serra do Mar and Parque Estadual de Ilhabela for allowing access and sampling in the conservation area. This research was financially supported by São Paulo Research Foundation (FAPESP Grants, #2012/15462-7 and #2016/06114-6), Conselho Nacional de Desenvolvimento Científico e Tecnológico (CNPq Grant, # 404767/2016-8) and CIC (University of Granada). The data used are listed in the references, tables and supporting information. This is the IBERSIMS publication n^{o} 20.

References

Aitken, A.R.A., Betts, P.G., & Ailleres L. (2009). The architecture, kinematics, and lithospheric processes of a compressional intraplate orogen occurring under Gondwana assembly: The Petermann orogeny, central Australia. *Lithosphere*, *1*, 343–357.

Aitken, A.R.A., Raimondo, T., & Capitanio, F.A. (2013). The intraplate character of supercontinent tectonics. *Gondwana Research*, *24*, 807–814.

Alkmim, F.F., Marshak, S., Pedrosa-Soares, A.C., Peres, G.G., Cruz, S.C.P., & Whittington, A. (2006). Kinematic evolution of the Araçuaí-West Congo orogen in Brazil and Africa: Nutcracker tectonics during the Neoproterozoic assembly of Gondwana. *Precambrian Research*, *149*, p. 43–64.

Almeida, F.F.M., Hasui, Y., Brito-Neves, B.B., & Fuck, R.A. (1981). Brazilian Structural Provinces: an introduction. *Earth-Science Reviews*, *17*, 1–29.

Almeida, R.P., Janikian, L., Fragoso-Cesar, A.R.S., & Fambrini, G.L. (2010). The Ediacaran to Cambrian Rift System of Southeastern South America: Tectonic Implications. *The Journal of Geology*, *118*, 145–161.

Almeida, R.P., Santos, M.G.M., Fragoso-Cesar, A.R.S., Janikian, L., & Fambrini, G.L. (2012). Recurring extensional and strike-slip tectonics after the Neoproterozoic collisional events in the southern Mantiqueira province. *Anais da Academia Brasileira de Ciências*, *84*, 347–376.

Alves, A., Janasi, V.A., & Campos Neto, M.C. (2016). Sources of granite magmatism in the Embu Terrane (Ribeira Belt, Brazil): Neoproterozoic crust recycling constrained by

elemental and isotope (Sr-Nd-Pb) geochemistry. *Journal of South American Earth Sciences*, *68*, 205–223.

Alves, A., Janasi, V.A., Campos Neto, M.C., Heaman, L., & Simonetti, A. (2013). U–Pb geochronology of the granite magmatism in the Embu Terrane: Implications for the evolution of the Central Ribeira Belt, SE Brazil. *Precambrian Research*, *230*, 1–12.

Beaumont, C., Jamieson, R.A., Nguyen, M.H., & Lee, B. (2001). Himalayan tectonics explained by extrusion of a low- viscosity crustal channel coupled to focused surface denudation. *Nature*, *414(6865)*, 738–742. doi:10.1038/414738a.

Beaumont C, Nguyen, M.H., Jamieson, R.A., & Ellis, S. (2006). Crustal flow modes in large hot orogens. In Law R.D, Searle, M.P., & Godin, L. (Eds.), *Channel Flow, Ductile Extrusion and Exhumation of Lower Mid-crust in Continental Collision Zones*, *Geological Society [London] Special Publication* (Vol. 268, pp. 91–145).

Black, L.P., Kamo, S.L., Allen, C.M., Aleinikoff, J.A., Davis, D.W., Korsch, J.R., & Foudolis, C. (2003). TEMORA 1: a new zircon standard for Phanerozoic U–Pb geochronology. *Chemical Geology*, *200*, 155–170.

Brito-Neves, B.B., & Cordani, U.G. (1991). Tectonic evolution of South America during Late Proterozoic. *Precambrian Research*, *33*, 23–40.

Brito-Neves, B.B., Campos Neto, M.C., & Fuck, R.A. (1999). From Rodinia to Western Gondwana: An approach to the Brasiliano-Pan African Cycle and orogenic collage. *Episodes*, *22*, 155–166.

Campanha, G.A.C, & Ens, H.H. (1996). Estruturação geológica da região da Serra do Juqueriquerê, São Sebastião, SP. *Boletim IG - Instituto de Geociências USP*, *27*, 41–49.

Campanha, G.A.C., & Sadowski, G.D. (1999). Tectonics of the southern portion of the Ribeira Belt (Apiaí Domain). *Precambrian Research*, *98*, 31–51.

Campos Neto, M.C. (2000). Orogenic systems from Southwestern Gondwana: an approach to Brasiliano–Pan African Cycle and orogenic collage in Southeastern Brazil. In Cordani, U.G., Milani, E.J., Thomaz Filho, A., & Campos, D.A. (Eds.), *Tectonic Evolution of South America* (pp. 335–368). Rio de Janeiro, Brazil: 31st International Geological Congress.

Campos Neto, M.C., Basei, M.A.S., Janasi, V.A., & Moraes, R. (2011). Orogen migration and tectonic setting of the Andrelândia Nappe system: An Ediacaran western Gondwana collage, south of São Francisco craton. *Journal of South American Earth Sciences*, *32*, 393–406.

Campos Neto, M.C., & Caby, R. (2000). Terrane accretion and upward extrusion of high-pressure granulites in the Neoproterozoic nappes of southeast Brazil: petrologic and structural constraints. *Tectonics*, *19*, 669–687.

Campos Neto, M.C., & Figueiredo, M.C.H. (1995). The Rio Doce Orogeny, Southeastern Brazil. *Journal of South American Earth Sciences*, *8*, 143–162.

Catlos, E., Jacob, L., Oyman, T., & Sorensen, S. (2012). Long-term exhumation of an aegean metamorphic core complex granitoids in the Northern Menderes Massif, Western Turkey. *American Journal of Science*, *312*, 534 –571.

Coggon, R. & Holland, T.J.B. (2002). Mixing properties of phengitic micas and revised garnet-phengite thermobarometers. *Journal of Metamorphic Geology*, *20*, 683–696.

Corfu F., Hanchar, J.M., Hoskin, P.W.O., & Kinny, P. (2003). Atlas of zircon textures. In Hanchar J.M., & Hoskin, P.W.O. (Eds.), *Zircon: Mineralogical Society of America, Reviews in Mineralogy* (Vol. 53, pp. 469–500).

Cunningham, D. (2005). Active intracontinental trans- pressional mountain building in the Mongolian Altai: Defining a new class of orogen. *Earth Planetary Science Letters*, *240*, 436–444.

Cunningham, D. (2013). Mountain building processes in intracontinental oblique deformation belts: Lessons from the Gobi Corridor, Central Asia. *Journal of Structural Geology*, *46*, 255–282.

de Capitani, C. & Brown, T.H. (1987). The computation of chemical equilibrium in complex sys- tems containing non-ideal solutions. *Geochimica et Cosmochimica Acta*, *51*, 2639–2652.

de Capitani, C. & Petrakakis, K. (2010). The computation of equilibrium assemblage diagrams with Theriak/Domino software. *American Mineralogist, 95*, 1006–1016.

Dewey, J.F., & Bird, J.M. (1970). Mountain Belts and the New Global Tectonics. *Journal of Geophysical Research, 75*, 2625–2647.

Dyksterhuis, S., & Müller, R.D. (2008). Cause and evolution of intraplate orogeny in Australia. *Geology*, *36*, 495–498.

Egydio-Silva, M., Vauchez, A., Raposo, M.I.R., Bascou, J., & Uhlein, A. (2005). Deformation regime variations in an arcuate transpressional orogen (Ribeira belt, SE Brazil) imaged by anisotropy of magnetic susceptibility in granulites. *Journal of Structural Geology*, *27*, 1750–1764.

Faleiros, F.M., Campanha, G.A.C., Martins, L., Vlach, S.R.F., & Vasconcelos, P.M. (2011). Ediacaran high-pressure collision metamorphism and tectonics of the southern Ribeira Belt (SE Brazil): evidence for terrane accretion and dispersion during Gondwana assembly. *Precambrian Research*, *189*, 263–291.

Fossen, H., Cavalcante, C., Almeida, R.P. (2017). Hot versus Cold Orogenic Behaviour: Comparing the Araçuaí-West Congo and the Caledonian Orogens. *Tectonics*, *36*. https://doi.org/10/1002/2017TC004743.

Ganade de Araujo, C.E., Rubatto, D., Hermann, J., Cordani, U.G., Caby, R., & Basei, M.A.S. (2014). Ediacaran megamountains: evidence for >2500-km-long deep continental subduction in the West Gondwana Orogen. *Nature Communications*. doi: 10.1038/ncomms6198.

Garcia-Casco, A. (2007). Magmatic paragonite in trondhjemites from the Sierra del Convento mélange, Cuba. *American Mineralogist*, *92*, 1232–1237.

Gordon, R.G. (1998). The Plate Tectonic approximation: Plate Nonridigity, Diffuse Plate Boundaries and Global Plate Reconstructions. *Annual Review Earth Planetary Science*, *26*, 615–642.

Hasui, Y., & Sadowski, G.R. (1976). Evolução geológica do Pré-Cambriano na região sudeste do Estado de São Paulo. *Revista Brasileira de Geociências*, 6, 182–200.

Heilbron, M., & Machado, N. (2003). Timing of terrane accretion in the Neoproterozoic–Eopaleozoic Ribeira belt, SE Brazil. *Precambrian Research*, *125*, 87–112.

Heilbron, M., Pedrosa-Soares, A.C., Campos Neto, M.C., Silva, L.C., Trouw, R.A.J., & Janasi, V.A. (2004). A Província Mantiqueira. In Mantesso-Neto, V., Bartorelli, A., Carneiro, C.D.R., & Brito-Neves, B.B. (Eds.), *O desvendar de um continente: a moderna geologia da*

América do Sul e o legado da obra de Fernando Flávio Marques de Almeida (pp. 203–234). São Paulo: Beca.

Heilbron, M., Tupinambá, M., Valeriano, C.M., Armstrong, R., Silva, L.G.E., Melo, R.S., Simonetti, A., Pedrosa-Soares, A.C., & Machado, N. (2013). The Serra da Bolívia complex: The record of a new Neoproterozoic arc-related unit at Ribeira belt. *Precambrian Research, 238*, 158–175.

Heilbron, M., Valeriano, C.M., Tassinari, C.C.G., Almeida, J.C.H., Tupinambá, M., Siga Jr, O., & Trouw, R.A.J. (2008). Correlation of Neoproterozoic terranes between Ribeira Belt, SE Brazil and its African counterpart: comparative tectonic evolution and open questions. In Pankhurst, R.J., Trouw, R.A.J., Brito-Neves, B.B., & de Wit, M.J. (Eds.), *West Gondwana: Pre-Cenozoic Correlations Across the South Atlantic Region*, *Geological Society [London] Special Publication* (Vol. 294, pp. 211–238).

Holland, T.J.B., & Powell, R. (1998). An internally consistent thermodynamic data set for phases of petrological interest. *Journal of Metamorphic Geology*, *16*, 309–343.

Holland, T.J.B., Baker, J., & Powell, R. (1998). Mixing properties and activity–composition relationships of chlorites in the system MgO–FeO–Al2O3–SiO2–H2O. *European Journal of Mineralogy*, *10*, 395–406.

Hoskin, P.W.O., & Schaltegger, U., 2003, The composition of zircon and igneous and metamorphic petrogenesis. In Hanchar J.M., & Hoskin, P.W.O. (Eds.), *Zircon: Mineralogical Society of America*, *Reviews in Mineralogy* (Vol. 53, pp. 27–62).

Howell, D.G. (1989). *Tectonics of suspect terranes: Mountain building and continental growth*. London: Chapman & Hall.

Jamieson, R.A., Unsworth, M.J., Harris, N.B.W., Rosenberg, C.L., & Schulmann, K. (2011). Crustal melting and the flow of mountains. *Elements*, *7*, 253–260.

Janasi, V.A., Leite, R.J., & Van Schmus, W.R. (2001). U−Pb chronostratigraphy of the granitic magmatism in the Agudos Grandes Batholith (West of São Paulo, Brazil) - implications for the evolution of the Ribeira Belt. *Journal of South American Earth Sciences*, *14*, 363–376.

Janasi, V.A., Vlach, S.R.F., Campos Neto, M.C., & Ulbrich, H.H.G.J. (2009). Associated A-type subalkaline and high-K calc-alkaline granites in the Itu Granite Province, southeastern Brazil: Petrological and Tectonic significance. *The Canadian Mineralogist*, *47*, 1505–1526.

Jones, D.L., Howell, D.G., Coney, P.J., & Monger, J.W.H. (1983). Recognition, character and analysis of tectonostratigraphic terranes in Western North America. In Hashimoto, M., & Uyeda, S. (Eds.), *Accrection tectonics in the Circum-Pacific regions* (pp. 21–35). Tokyo: TERRAPUB.

Juliani, C., & Beljavskis, P. (1995). Revisão da litoestratigrafia da Faixa São Roque/Serra do Itaberaba (SP). *Revista do Instituto Geológico*, *16*, 33–58.

Juliani, C., Hackspacher, P., Dantas, E.L., & Fetter, A.H. (2000). The mesoproterozoic volcano-sedimentary Serra do Itaberaba Group of the Central Ribeira Belt, São Paulo State, Brazil: implications for the age of the overlying São Roque Group. *Revista Brasileira de Geociências*, 30, 82–86.

Konstantinou, A., Strickland, A., Vervoort, E.M.J., Fisher, C.M., Wooden, J., & Valley, J. (2013). Synextensional magmatism leading to crustal flow in the Albion–Raft River–Grouse Creek metamorphic core complex, northeastern Basin and Range. *Tectonics*, *32*, 1384–1403.

Kruckenberg, S.C., Ferré, E.C., Teyssier, C., Vanderhaeghe, O., Whitney, D.L., Seaton, N.C.A., & Skord, J.A. (2010). Viscoplastic flow in migmatites deduced from fabric anisotropy: An example from the Naxos dome, Greece. *Journal of Geophysical Research, 115*, B09401. doi:10.1029/2009JB007012.

Kruckenberg, S.C., Vanderhaeghe, O., Ferré, E.C., Teyssier, C., & Whitney, D.L. (2011). Flow of partially molten crust and the internal dynamics of a migmatite dome, Naxos, Greece. *Tectonics, 30*, TC3001. doi:10.1029/2010TC002751.

Lenz, C., Fernandes, L.A.D., McNaughton, N.J., Porcher, C.C., & Masquelin, H. (2011). U–Pb SHRIMP ages for the Cerro Bori Orthogneisses, Dom Feliciano Belt in Uruguay: Evidences of a ~800 Ma magmatic and ~650 Ma metamorphic event. *Precambrian Research, 185*, 149–163.

Matte, P. (2001). The Variscan collage and orogeny (480–290 Ma) and the tectonic definition of the Armorica microplate: a review. *Terra Nova, 13*, 122–128.

McFadden, R.R., Siddoway, C.S., Teyssier, C., & Fanning, C.M. (2010a). Cretaceous oblique extensional deformation and magma accumulation in the Fosdick Mountains migmatite-cored gneiss dome, West Antarctica. *Tectonics, 29*, TC4022. doi:10.1029/2009TC002492.

McFadden, R.R., Teyssier, C., Siddoway, C.S., Whitney, D.L., & Fanning, C.M. (2010b). Oblique dilation, melt transfer, and gneiss dome emplacement. *Geology, 38*, 375–378.

McKenzie, D., & Parker, R.L. (1967). The North Pacific: an example of tectonics on a sphere. *Nature, 216*, 1276–1280.

Meira V.T. (2014). *Evolução tectono-metamórfica neoproterozoica dos complexos Costeiro e Embu no contexto de formação do Gondwana Ocidental (Leste do Estado de São Paulo)* (doctoral thesis). Retrieved from Teses USP. (http://www.teses.usp.br/teses/disponiveis/44/44141/tde-03062015-150734/pt-br.php). São Paulo, Brazil: Institute of Geosciences, University of São Paulo.

Meira, V.T., Garcia-Casco, A., Juliani, C., Almeida, R.P., & Schorscher, J.H.D. (2015). The role of intracontinental deformation in supercontinent assembly: insights from the Ribeira Belt, Southeastern Brazil (Neoproterozoic Western Gondwana). *Terra Nova, 27*, 206–217.

Meira, V.T., Juliani, C., Schorscher, J.H.D., Garcia-Casco, A., & Hyppolito, T. (2014). *Does the Pico do Papagaio Batholith indeed represent a Neoproterozoic Magmatic Arc?* Paper presented at 9th South American Symposium on Isotope Geology, São Paulo, Brazil.

Morgan, W.J. (1968). Rises, Trenches, Great Faults, and Crustal Blocks. *Journal of Geophysical Research, 73*, 1959–1982.

Neves, S.P. (2003). Proterozoic history of the Borborema Province (NE Brazil): correlations with neighboring cratons and Pan-African belts, and implications for the evolution of western Gondwana. *Tectonics, 22*, 1031. doi:10.1029/2001TC001352.

Neves, S.P., Tommasi, A., Vauchez, A., & Hassani, R. (2008). Intraplate continental deformation: Influence of a heat-producing layer in the lithospheric mantle. *Earth and Planetary Science Letters, 274*, 392–400.

Norlander, B.H., Whitney, D.L., Teyssier, C., & Vanderhaeghe, O. (2002). Partial melting and decompression of the Thor-Odin dome, Shuswap metamorphic core complex, Canadian Cordillera. *Lithos, 61*, 103–125.

Powell, R., & Holland, T.J.B. (1994). Optimal geothermometry and geobarometry. *American Mineralogist, 79*, 120–133.

Powell, R., & Holland, T.J.B. (1999). Relating formulations of the thermodynamics of mineral solid solutions: Activity modeling of pyroxenes, amphiboles, and micas. *American Mineralogist*, *84*, 1–14.

Raimondo, T., Collins, A.S., Hand, M., Walker-Hallam, A., Smithies, R.H., Evins, P.M., & Howard, H.M. (2009). Ediacaran intracontinental channel flow. *Geology*, *37*, 291–294.

Raimondo, T., Collins, A.S., Hand, M., Walker-Hallam, A., Smithies, R.H., Evins, P.M., & Howard, H.M. (2010). The anatomy of a deep intracontinental orogen. *Tectonics*, *29*, TC4024. doi:10.1029/2009TC002504.

Raimondo, T., Hand, M., & Collins, W.J. (2014). Compressional intracontinental orogens: Ancient and modern perspectives. *Earth-Science Reviews*, 130, 128–153.

Reno, B.L., Piccoli, P.M., Brown, M., & Trouw, R.A.J. (2012). *In situ* monazite (U–Th)–Pb ages from the Southern Brasília Belt, Brazil: constraints on the high-temperature retrograde evolution of HP granulites. *Journal of Metamorphic Geology*, *30*, 81–112.

Rey, P.F., Teyssier, C., Kruckenberg, S.C., & Whitney, D.L. (2011). Viscous collision in channel explains double domes in metamorphic. *Geology*, 39, 387–390.

Rey, P.F., Teyssier, C., & Whitney, D.L. (2009a). Extension rates, crustal melting, and core complex dynamics. *Geology*, *37*, 391–394.

Rey, P.F., Teyssier, C., & Whitney, D.L. (2009b). The role of partial melting and extensional strain rates in the development of metamorphic core complexes. *Tectonophysics*, *477*, 135–144.

Rocha, B.C., Moraes, R., Moller, A., Cioffi, C.R. (2018). Magmatic inheritance vs. UHT metamorphism: Zircon petrochronology of granulites and petrogenesis of charnockitic leucosomes of the Socorro-Guaxupé nappe, SE Brazil. *Lithos*, *314–315*, 16–39.

Rogers, J.J.W., & Santosh, M. (2003). Supercontinents in earth history. *Gondwana Research*, *6*, 357–368.

Rubatto, D. (2002). Zircon trace element geochemistry: distribution coefficients and the link between U-Pb ages and metamorphism. *Chemical Geology*, *184*, 123–138.

Santosh, M., Maruyama, S., & Yamamoto, S. (2009). The making and breaking of supercontinents: some speculations based on superplumes, super downwelling and the role of tectosphere. *Gondwana Research*, *15*, 324–341.

Sawyer, E.W. (2008). Atlas of migmatites. *The Canadian Mineralogist Special Publications* (Vol. 9). Ottawa, Ontario: NRC Research Press.

Schaltegger, U., Fanning, M., Günther, D., Maurin, J.C., Schulmann, K., & Gebauer, D. (1999). Growth, annealing and recrystallization of zircon and preservation of monazite in high-grade metamorphism: conventional and in-situ U–Pb isotope, cathodoluminescence and microchemical evidence. *Contributions to Mineralogy and Petrology*, *134*, 186–201.

Sengör, A.M.C. (1990). Plate Tectonics and Orogenic Research after 25 years: A Tethyan Perpective *Earth-Science Reviews*, *27*, 1–201.

Shaw, R.D., Etheridge, M.A., & Lambeck, K. (1991). Development of the Late Proterozoic to Mid Paleozoic, Intracratonic Amadeus Basin in central Australia: A key to understanding tectonic forces in plate interiors. *Tectonics*, *10*, 688–721.

Siga Jr., O., Basei, M.A.S., Nutman, A., Sato, K., McReath, I., Passarelli, C.R., & Liu, D. (2011). Extensional and Colisional Magmatic Records in the Apiaí Terrane, South-

Southeastern Brazil: Integration of Geochronological U-Pb Zircon Ages. *Geologia USP*, *11*, 149–175.

Silva, L.C., McNaughton, N., Armstrong, R., Hartmann, L., & Fletcher, I. (2005). The Neoproterozoic Mantiqueira Province and its African connections. *Precambrian Research*, *136*, 203–240.

Spear, F.S., Kohn, M.J., & Cheney, J.T. (1999). P -T paths from anatectic pelites. *Contributions to Mineralogy and Petrology*, *134*, 17–32.

Spencer, C. J., Kirkland, C. L., & Taylor, R. J. M. (2016). Strategies towards statistically robust interpretations of in situ U-Pb zircon geochronology. *Geoscience Frontiers*, *7*, 581–589.

Tedeschi, M., Lanari, P., Rubatto, D., Pedrosa-Soares, A.C., Hermann, J., Dussin, I., Pinheiro, M.A.P., Bouvier, A.S., Baumgartner, L. (2017). Reconstruction of multiple P-T-t stages from retrogressed mafic rocks: Subduction vs collision in the Southern Brasília orogen (SE Brazil). *Lithos*, *294–295*, 283–303.

Tedeschi, M., Pedrosa-Soares, A.C., Dussin, I., Lanari, P., Novo, T., Pinheiro, M.A.P., Lana, C., Peters, D. (2018). Protracted zircon geochronological record of UHT garnet-free granulites in the Southern Brasília orogen (SE Brazil): petrochronological constraints on magmatism and metamorphism. Precambrian Research, doi: https//doi.org/10.1016/j.precamres.2018.07.023, in press.

Teyssier, C., & Whitney, D.L. (2002). Gneiss domes and orogeny. *Geology*, *30*, 1139–1142.

Tirel, C., Brun, J.- P., & Burov, E. (2004). Thermomechanical modeling of extensional gneiss domes. In Whitney, D.L., Teyssier, C., & Siddoway, C.C. (Eds.), *Gneiss Domes in Orogeny*, *Geological Society of America Special Paper* (Vol. 380, pp. 67–78). Boulder, CO: GSA.

Tommasi A., & Vauchez, A. (1997). Continental-scale rheological heterogeneities and complex intraplate tectono-metamorphic patterns: insights from a case-study and numerical models. *Tectonophysics*, *279*, 327–350.

Torres-Roldán, R.L., Garcia-Casco, A., & Garcia-Sánchez, P.A. (2000). CSpace: an integrated workplace for the graphical and algebraic analysis of phase assemblages on 32-bit Wintel platforms. *Computers and Geosciences*, *26*, 779–793.

Trouw, R.A.J., Heilbron, M., Ribeiro, A., Paciullo, F.V.P., Valeriano, C.M., Almeida, J.C.H., Tupinambá, M., & Andreis, R.R. (2000). The central segment of the Ribeira Belt. In Cordani, U.G., Milani, E.J., Thomaz Filho, A., & Campos, D.A. (Eds.), *Tectonic Evolution of South America* (pp. 287–310). Rio de Janeiro, Brazil: 31st International Geological Congress.

Trouw, R.A.J., Peternel, R., Ribeiro, A., Heilbron, M., Vinagre, R., Duffles, P., Trouw, C.C., Fontainha, M., & Kussama, H.H. (2013). A new interpretation for the interference zone between the southern Brasília belt and the central Ribeira belt, SE Brazil. *Journal of South American Earth Sciences*, *48*, 43–57.

Tupinambá, M., Heilbron, M., Valeriano, C.M., Porto Júnior, R., Blanco de Dios, F., Machado, N. , Silva, L.G.E., & Almeida, J.C.H. (2012). Juvenile contribution of the Neoproterozoic Rio Negro Magmatic Arc (Ribeira Belt, Brazil): Implications for Western Gondwana amalgamation. *Gondwana Research*, *21*, 422–438.

Vanderhaeghe, O., & Teyssier, C. (2001). Partial melting and flow of orogens. *Tectonophysics*, *342*, 451–472.

Vauchez, A., Neves, S.P., Caby, R., Corsini, M., Egydio-Silva, M., Arthaud, M., & Amaro, V. (1995). The Borborema shear zone system. *Journal of South American Earth Sciences*, *8*, 247–266.

Vauchez, A., Tommasi, A., & Egydio-Silva, M. (1994). Self-indentation of continental lithosphere. *Geology*, *22*, 967–970.

Vermeesch, P. (2018). IsoplotR: A free and open toolbox for geochronology. *Geoscience Frontiers*, *9*, 1479–1493.

Vlach, S.R.F., Siga Jr, O., Harara, O.M.M., Gualda, G.A.R., Basei, M.A.S., & Vilalva, F.C.J. (2011). Crystallization ages of the A-type magmatism of the Graciosa Province (Southern Brazil): Constraints from zircon U−Pb (ID-TIMS) dating of coeval K-rich gabbro-dioritic rocks. *Journal of South American Earth Sciences*, *32*, 407–415.

White, R.W., Powell, R., Holland, T.J.B., & Worley, B.A. (2000). The effect of TiO2 and Fe2O3 on metapelitic assemblages at greenschist and amphibolite facies conditions: mineral equilibria calculations in the system K2O–FeO–MgO–Al2O3–SiO2–H2O–TiO2–Fe2O3. *Journal of Metamorphic Geology*, *18*, 497–511.

White, R.W., Powell, R. & Clarke, G.L. (2002). The interpretation of reaction textures in Fe-rich metapelitic granulites of the Musgrave Block, central Australia: Constraints from mineral equilibria calculations in the system K2O-FeO-MgO-Al2O3-SiO2-H2O-TiO2-Fe2O3. *Journal of Metamorphic Geology*, *20*, 41–55.

White, R.W., Pomroy, N.E. & Powell, R. (2005). An *in situ* metatexite-diatexite trasition in upper amphibolite facies rocks from Broken Hill, Australia. *Journal of Metamorphic Geology*, *23*, 579–602.

White, R.W., Powell, R. & Holland, T.J.B. (2007). Progress relating to calculation of partial melting equilibria for metapelites. *Journal of Metamorphic Geology*, *25*, 511–527.

Whitney, D.L., & Evans, B.W. (2010). Abbreviations for names of rock-forming minerals. *American Mineralogist*, *95*, 185–187.

Whitney, D.L., Teyssier, C., Fayon, A.K., Hamilton, M.A., & Heizler, M. (2003). Tectonic controls on metamorphism, partial melting, and intrusion: timing and duration of regional metamorphism and magmatism in the Nigde Massif, Turkey. *Tectonophysics*, *376*, 37–60.

Whitney, D.L., Teyssier, C., Rey, P., & Buck, W.R. (2013). Continental and oceanic core complexes. *GSA Bulletin*, *125*, 273–298.

Whitney, D.L., Teyssier, C., & Vanderhaeghe, O. (2004). Gneiss domes and crustal flow. In Whitney, D.L., Teyssier, C., & Siddoway, C.C. (Eds.), *Gneiss Domes in Orogeny*, *Geological Society of America Special Paper* (Vol. 380, pp. 15–33). Boulder, CO: GSA.

Wilson, J.T. (1965). A new class of faults and their bearing on continental drift. *Natur*e, *207*, 343–347.

Ziegler, P.A., Cloetingh, S., & van Wees, J.D. (1995). Dynamics of intra-plate compressional deformation: the Alpine foreland and other examples. *Tectonophysics*, *252*, 7–59.

Table 1. Summary of THERMOCALC optimal average *P–T* estimates (Holland and Powell, 1998) for each studied sample.

Sample	Rock type	Selected assemblage	*P–T* stage	Average T ±1σ (°C)	Average P ±1σ (kbar)	Correl.	Sig fit	sd(fit)
			Embu Complex					
PSM-111B	St-Grt-bearing mica schist	Grt/St/Bt/Ms/Qz/H2O	Peak	604±76	9.6±2.0	-0.165	1.35	1.54
PSM-111B	St-Grt-bearing mica schist	Grt/St/Bt/Ms/Qz/H2O	Peak	611±72	8.9±1.9	-0.227	1.25	1.54
PSM-111B	St-Grt-bearing mica schist	Grt/Bt/Ms/Chl/Pl/Qz/H2O	Retro	558±13	4.2±1.2	0.541	0.74	1.54
PSM-111B	St-Grt-bearing mica schist	Grt/Bt/Ms/Chl/Pl/Qz/H2O	Retro	560±14	4.0±1.3	0.581	0.63	1.54
PSM-111B	St-Grt-bearing mica schist	Grt/Bt/Ms/Chl/Pl/Qz/H2O	Retro	558±13	4.1±1.2	0.544	0.75	1.54
PSM-75C	Foliated metagranite	Grt/Bt/Ms/Chl/Pl/Qz/H2O	Retro	539±14	2.8±0.8	0.727	1.00	1.49
PSM-75C	Foliated metagranite	Grt/Bt/Ms/Chl/Pl/Qz/H2O	Retro	530±16	2.2±0.9	0.785	1.12	1.45
PSM-75C	Foliated metagranite	Grt/Bt/Ms/Chl/Pl/Qz/H2O	Retro	533±15	3.0±0.9	0.690	1.18	1.45
PSM-75C	Foliated metagranite	Grt/Bt/Ms/Chl/Pl/Qz/H2O	Retro	530±16	2.5±0.9	0.744	1.13	1.45
			Costeiro Complex					
PSM-104A1	Metatexitic metapelite	Grt/Bt/Sil/Pl/Qz/H2O	Peak	643±141	3.5±1.8	0.733	0.25	1.96
PSM-104A1	Metatexitic metapelite	Grt/Bt/Sil/Pl/Qz/H2O	Peak	621±135	3.4±1.8	0.707	0.19	1.96
PSM-104A1	Metatexitic metapelite	Grt/Bt/Sil/Pl/Qz/H2O	Peak	637±139	3.5±1.8	0.730	0.24	1.96
PSM-104D	Metatexitic metapelite	Grt/Bt/Ms/Pl/Qz/H2O	Peak	733±40	6.8±1.4	0.689	1.14	1.54
PSM-104D	Metatexitic metapelite	Grt/Bt/Ms/Pl/Qz/H2O	Peak	735±38	6.9±1.3	0.691	1.09	1.54
PSM-104D	Metatexitic metapelite	Grt/Bt/Ms/Pl/Qz/H2O	Retro	700±47	5.4±1.7	0.734	1.22	1.73
PSM-104D	Metatexitic metapelite	Grt/Bt/Ms/Pl/Qz/H2O	Retro	696±46	5.5±1.6	0.736	1.23	1.73
PSM-104D	Metatexitic metapelite	Grt/Bt/Ms/Pl/Qz/H2O	Retro	719±40	5.5±1.3	0.710	0.84	1.54
PSM-109E	Metatexitic metapelite	Grt/Bt/Sil/Pl/Qz/H2O	Peak	597±125	4.1±1.8	0.753	0.32	1.96
PSM-109E	Metatexitic metapelite	Grt/Bt/Sil/Pl/Qz/H2O	Peak	592±125	4.5±1.8	0.770	0.33	1.96
PSM-60B	Amp-bearing Grt-Bt paragneiss	Grt/Amp (Ts)/Bt/Pl/Qz/H2O	Peak	656±73	3.6±1.2	0.389	0.78	1.61
PSM-60B	Amp-bearing Grt-Bt paragneiss	Grt/Amp (Ts)/Bt/Pl/Qz/H2O	Peak	641±71	3.6±1.2	0.390	0.93	1.61
PSM-61A	Grt-Bt-bearing amphibolite	Grt/Amp (Fe-Ts)/Bt/Pl/Qz/H2O	Peak	622±72	4.7±1.2	0.444	1.07	1.61
PSM-61A	Grt-Bt-bearing amphibolite	Grt/Amp (Fe-Ts)/Bt/Pl/Qz/H2O	Peak	623±67	4.8±1.1	0.449	0.97	1.61
PSM-	Grt-Bt-bearing	Grt/Amp (Cum-	Retro	464±67	3.5±0.7	0.160	1.01	1.94

61A	amphibolite	Gru)/Bt/Pl/Qz/H2O				2	6	6
PSM-61A	Grt-Bt-bearing amphibolite	Grt/Amp (Cum-Gru)/Bt/Pl/Qz/H2O	Retro	460±62	3.3±0.6	0.11 9	0.9 9	1.9 6
PSM-61B	Grt-Bt-bearing amphibolite	Grt/Amp (Cum-Gru)/Chl/Pl/Qz/H2O	Retro	576±25	3.6±1.4	0.48 2	1.8 8	1.7 3
PSM-61B	Grt-Bt-bearing amphibolite	Grt/Amp (Mg-Hbl)/Chl/Pl/Qz/H2O	Retro	550±16	3.9±1.1	0.36 8	1.2 3	1.6 1
PSM-106A	Grt-Bt-bearing amphibolite	Grt/Amp (Fe-Ts)/Bt/Pl/Qz/H2O	Peak	743±88	5.5±1.3	0.48 7	1.0 2	1.4 9
PSM-106A	Grt-Bt-bearing amphibolite	Grt/Amp (Fe-Ts)/Bt/Pl/Qz/H2O	Peak	711±81	5.6±1.2	0.49 9	0.7 6	1.5 4
PSM-106A	Grt-Bt-bearing amphibolite	Grt/Amp (Mg-Hbl)/Bt/Chl/Pl/Qz/H2O	Retro	539±12	4.7±0.8	0.22 5	0.9 9	1.4 9
PSM-106A	Grt-Bt-bearing amphibolite	Grt/Amp (Mg-Hbl)/Bt/Chl/Pl/Qz/H2O	Retro	536±12	4.5±0.8	0.24 0	1.0 2	1.4 9
PSM-106D	Grt-Bt-bearing amphibolite	Grt/Amp (Fe-Ts)/Bt/Pl/Qz/H2O	Peak	746±102	4.9±1.4	0.41 9	1.0 8	1.6 1
PSM-106D	Grt-Bt-bearing amphibolite	Grt/Amp (Fe-Ts)/Bt/Pl/Qz/H2O	Peak	732±90	4.3±1.3	0.41 2	0.8 7	1.6 1
PSM-106D	Grt-Bt-bearing amphibolite	Grt/Amp (Fe-Ts)/Bt/Pl/Qz/H2O	Peak	755±97	4.6±1.3	0.40 8	0.9 0	1.6 1
PSM-106D	Grt-Bt-bearing amphibolite	Grt/Amp (Fe-Ts)/Bt/Pl/Qz/H2O	Peak	734±90	4.6±1.3	0.42 6	0.9 5	1.6 1
PSM-106D	Grt-Bt-bearing amphibolite	Grt/Amp (Mg-Hbl)/Bt/Pl/Qz/H2O	Retro	612±103	4.1±1.6	0.42 3	1.4 9	1.6 1
PSM-106D	Grt-Bt-bearing amphibolite	Grt/Amp (Mg-Hbl)/Bt/Pl/Qz/H2O	Retro	621±97	4.1±1.5	0.42 7	1.3 7	1.6 1

Note. Abbreviations throughout the manuscript follow Whitney and Evans (2010).

Table 2. Mineral Abundance of the Studied Samples (visual estimates).

Sample	Rock type	Grt	Amp	Sil	St	Bt	Ms	Chl	Qz	Pl	Kfs	Ilm
					Embu Complex							
PSM-75C	Foliated metagranite	2				20	35	8	20	15	x	x
PSM-111B	St-Grt-bearing mica schist	5			10	30	40	5	10	x		x
					Costeiro Complex							
					Metasedimentary rocks							
PSM-60B	Amp-bearing Grt-Bt paragneiss	5	3			25			30	32		5
PSM-104A1	Metatexitic metapelite	5		20		30	x		25	20	x	x
PSM-104D	Metatexitic metapelite	3		7		10	3		30	25	20	x
PSM-109E	Metatexitic metapelite	3		5		15			40	35	x	x
					Amphibolites							
PSM-61A	Grt-Bt-bearing amphibolite	8	35			10		x	5	30		10
PSM-61B	Grt-Bt-bearing amphibolite	2	55			x			10	15		15
PSM-106A	Grt-Bt-bearing amphibolite	15	10			7			35	30		3
PSM-106D	Grt-Bt-bearing amphibolite	15	25			20			15	20		5

x: Present in small amounts.

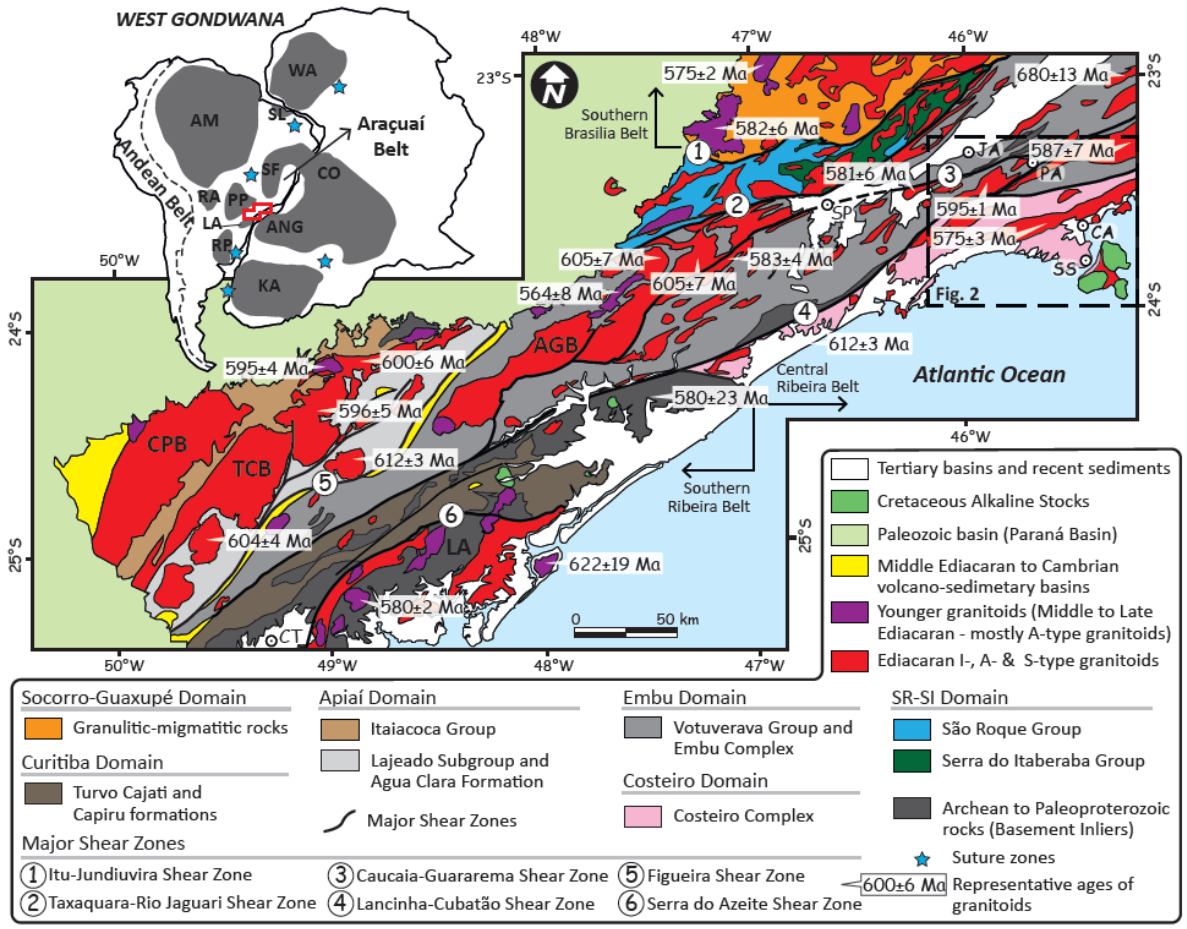

Figure 1. Regional geologic map of Southern and Central Ribeira Belt, showing major shear zones and available ages of magmatic bodies indicated. The inset shows the cratonic blocks of West Gondwana. Evidence for suture zones includes ophiolites, well-defined magmatic arcs and high-pressure rocks. Abbreviations: Cities – CA, Caraguatatuba; CT, Curitiba; JA, Jacareí; PA, Paraibuna; SP, São Paulo; SS, São Sebastião; Batholiths – AGB, Agudos Grandes Batholith; CPB, Cunhaporanga Batholith; TCB, Três Córregos Batholith; Cratons – AM, Amazonia Craton; ANG, Angola Block; CO, Congo Craton; KA, Kalahari Craton; LA, Luis Alves Craton; PP, Paranapanema Block; RA, Rio Apa Block; RP, Rio de La Plata Craton; SL, São Luis Craton; WA, West Africa Craton.

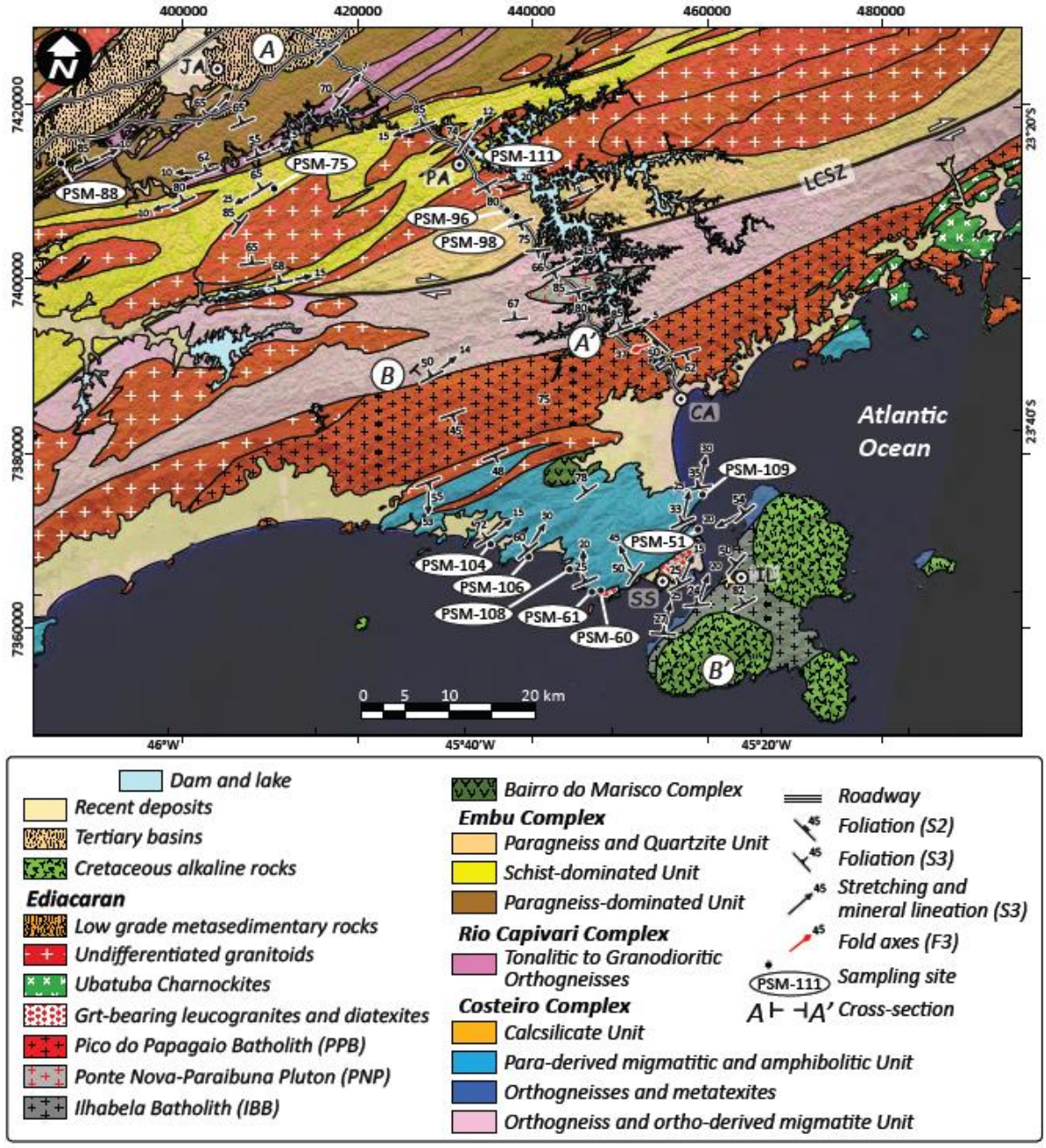

Figure 2. Geological map of the studied area. See location in Figure 1. All sampling sites are shown. Abbreviations: Cities – CA, Caraguatatuba; IL, Ilhabela; JA, Jacareí; PA, Paraibuna; SS, São Sebastião. LCSZ, Lancinha-Cubatão Shear Zone.

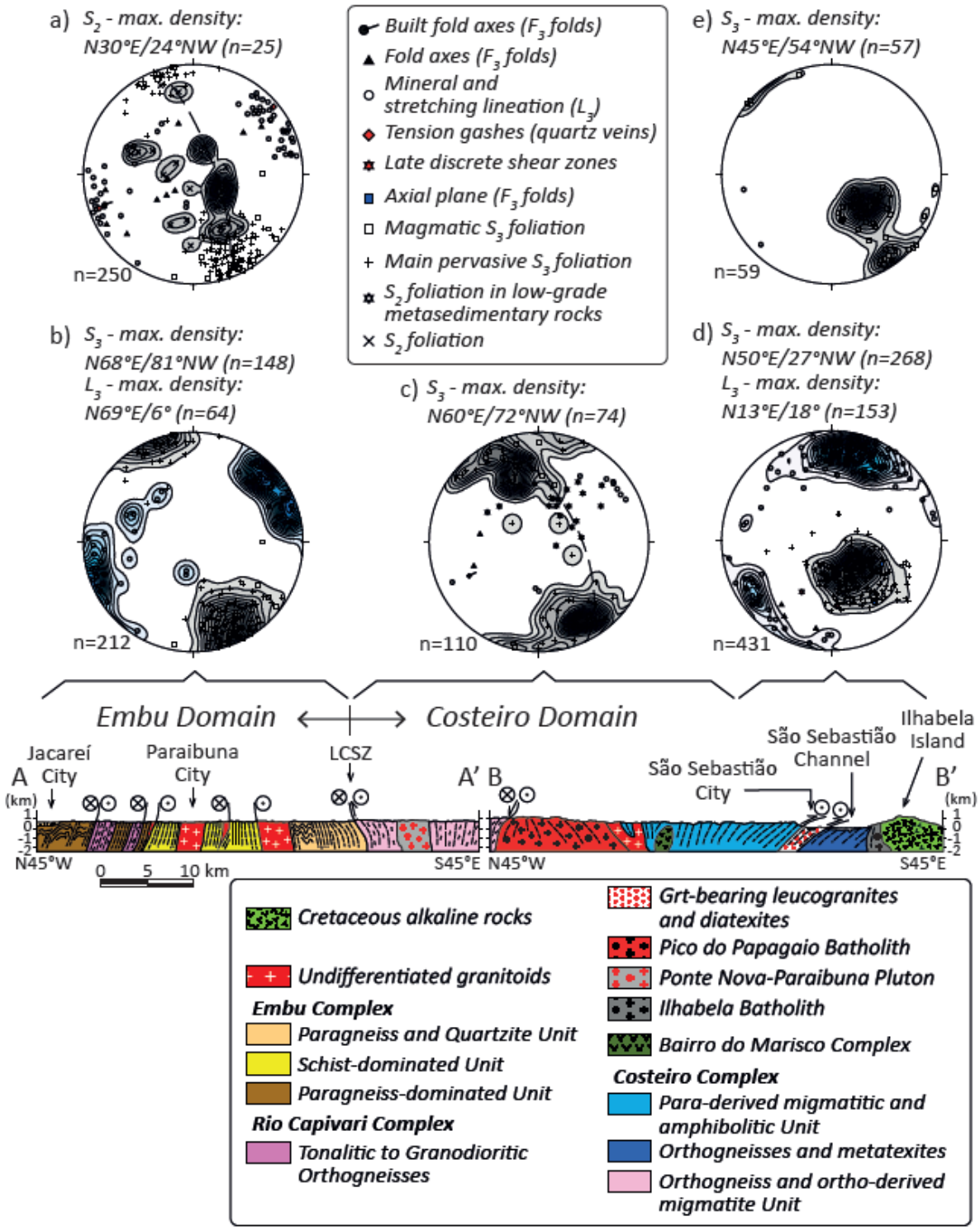

Figure 3. Schematic geological cross-section through the studied area and lower hemisphere equal area stereographic projections of all structural data collected in this work. See Figure 2 for location of cross-sections A-A' and B-B'. (a) and (b) Structural data from Embu Domain. Grey contoured density in (a) represents S2 folded foliation and grey and blue contoured densities in (b) represent S3 foliation and L3 stretching and mineral lineations, respectively. (c) Structural data from western part of Costeiro Domain. Note the northeast-directed doming structure, well delineated in the structures of the Pico do Papagaio Batholith (PPB). (d) and (e) Structural data from eastern part of Costeiro Domain. (d) data from São Sebastião surroundings and (e) data from Ilhabela island. Abbreviation: LCSZ, Lancinha-Cubatão Shear Zone.

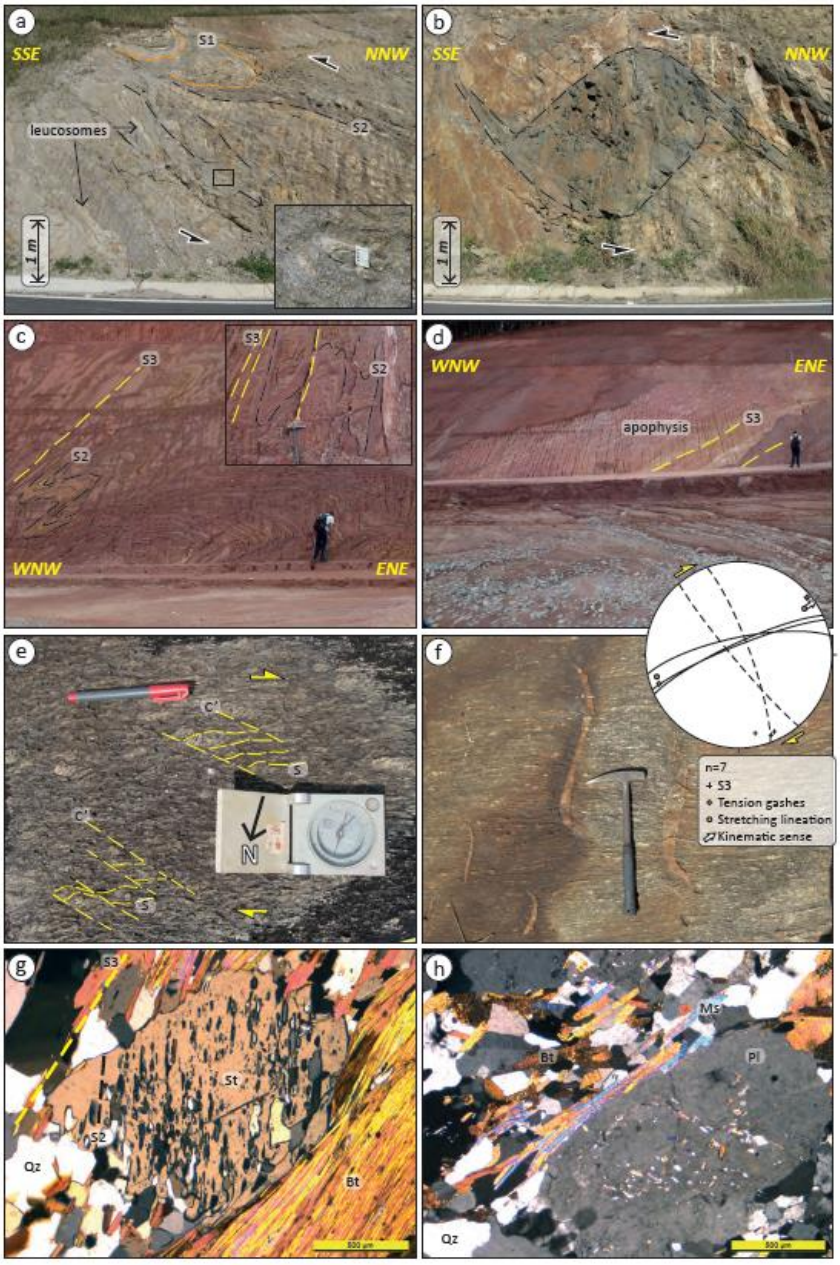

Figure 4. Main structural features of the Embu Domain. (a) Relics of S1 foliation defined by rootless intrafolial isoclinal F2 folds in para-derived metatexitic sequence of the Embu Complex (Paragneiss-dominated Unit). S/C and sigmoidal structures suggest top-to-the S-SSW sense of movement during D2 deformational phase. The inset highlights rootless isoclinal F2 fold defined by a quartzite layer. (b) Sigmoidal boudin of mafic rock interleaved with metatexitic paragneisses of the Embu Complex (Paragneiss-dominated Unit) as a δ-type kinematic indicator suggesting top-to-the S-SW sense of movement during the D2 deformational phase. (c) Asymmetric to upright F3 folds are transposed by S3 steep foliation in mica schists of the Embu Complex (Schist-dominated Unit). The inset image shows detail of the tight upright F3 folds and the axial plane S3 foliation (PSM-98). (d) Intrusive relationship of foliated granitic apophysis within schists of the Embu Complex (Schist-dominated Unit – PSM-98). Note that the foliation in the granitic apophysis is subconcordant to the S3 foliation of the host rocks. (e) and (f) S/C' structures and tension gashes filled by quartz veins, respectively, in porphyritic granites (borders of the Itapeti Pluton) suggesting dextral kinematics during high temperature solid-state deformation. Lower hemisphere equal area stereogram shows the main structural features of the deformed porphyritic granite. (g) Staurolite porphyroblast with relict internal S2 foliation wrapped by mica-rich bands that delineate the S3 mylonitic foliation (porphyroblastic St-Grt-bearing mica schist-PSM-111B – Embu Complex/Schist-dominated Unit, cross-polarized light). (h) Magmatic foliation defined by aligned muscovite, biotite and feldspar megacrysts in porphyritic peraluminous granite (Salesópolis Granite; cross-polarized light).

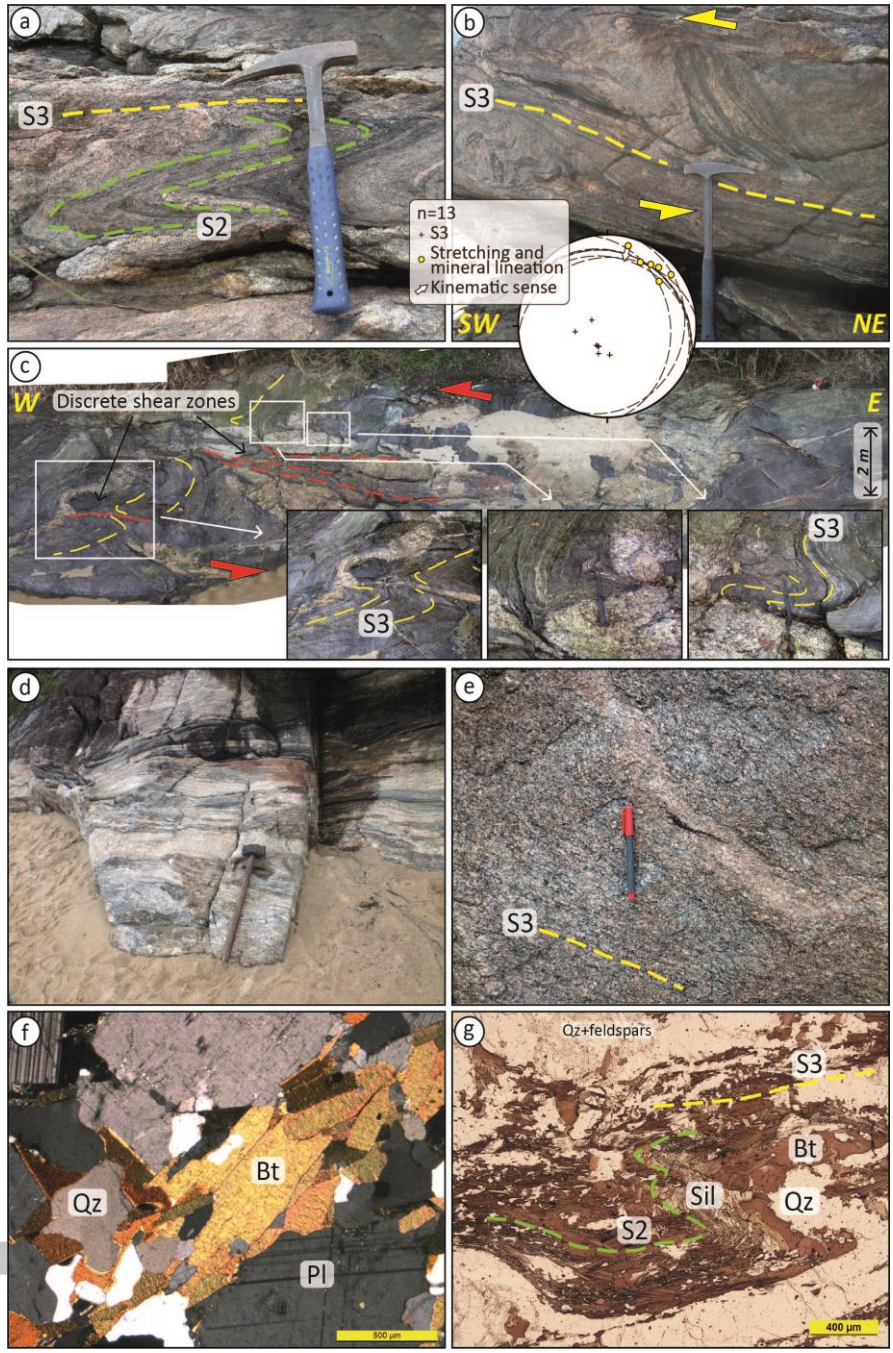

Figure 5. Main structural features of the Costeiro Domain. (a) Rootless isoclinal intrafolial F3 fold in metatexitic paragneiss of the Costeiro Complex (Para-derived migmatitic and amphibolitic Unit – PSM-61). (b) Kinematic indicators related to the S3 foliation, including sigmoidal schollen and asymmetric folds in metatexitic paragneiss of the Costeiro Complex (Para-derived migmatitic and amphibolitic Unit – PSM-61). Lower hemisphere equal area stereogram showing the main elements of the D3-related structures. (c) Photo mosaic of a coastal outcrop showing discrete shear zones filled with leucocratic veins. The inset images highlight the drag folds (para-derived migmatitic and amphibolitic Unit – PSM-60). (d) Stromatic metatexites with leucosome, neosome and amphibolitic boudins parallelized along the S3 foliation. Note the steeper dipping of the S3 foliation at this location (para-derived migmatitic and amphibolitic Unit – PSM-104). (e) Foliated homogeneous diatexite with schlieren and hololeucocratic veins. (f) Photomicrograph of biotitic schlieren in diatexite related to the magmatic foliation and aligned parallel to the regional S3 foliation. (g) Photomicrograph of F3 microfolds delineated by aggregates of sillimanite and biotite wrapped by S3 main foliation in medium- to fine-grained Sil-bearing Grt-Bt migmatitic paragneiss (metapelitic group – PSM-104A1). The quartzofeldspathic bands (leucosome) are oriented parallel to the S3 foliation.

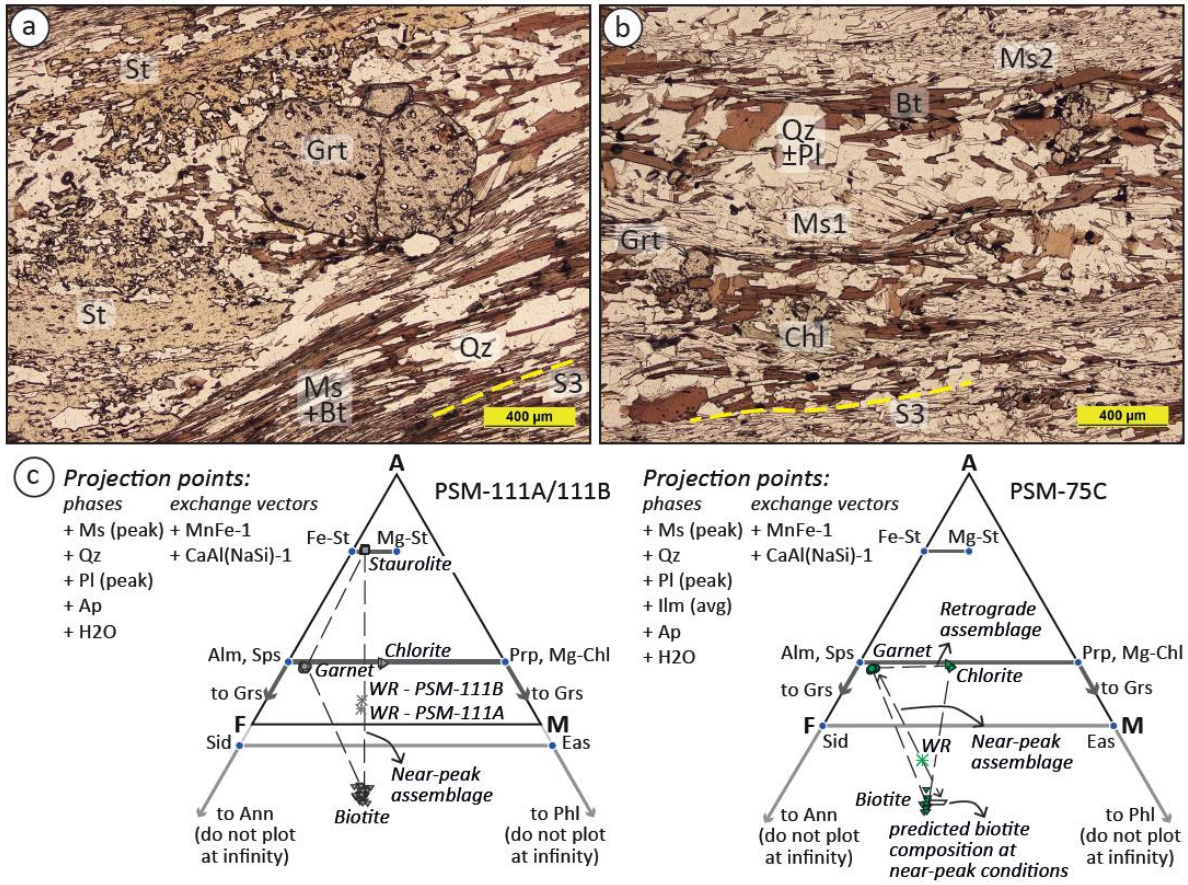

Figure 6. Transmitted light photomicrographs of petrological relationships and AFM compatibility diagrams of the Embu Complex. (a) Porphyroblastic St-Grt-bearing mica schist (PSM-111B) showing pre-S3 poikiloblastic St porphyroblasts and idioblastic to subidioblastic Grt porphyroblast wrapped by S3 mylonitic foliation, delineated by fine-grained Ms+Bt-rich and quartz-ribbon bands. The images are in plane-polarized light. (b) Fine-grained garnet-bearing mica-rich mylonite (mylonitic metagranite, PSM-75C) showing two phases of muscovite growth: an early phase of coarse-grained (Ms1 − mica-fish) grains (pre-S3 foliation) and the syn-mylonitic late fine-grained (Ms2) grains (S3 folation). Fine-grained garnet grains are chloritized and chlorite appears as retrograde post-S3 phase. Ms2 and Bt define the S3 mylonitic foliation. (c) AFM compatibility diagrams of metasedimentary rocks from Embu Complex (left) and mylonitized metagranite (right).

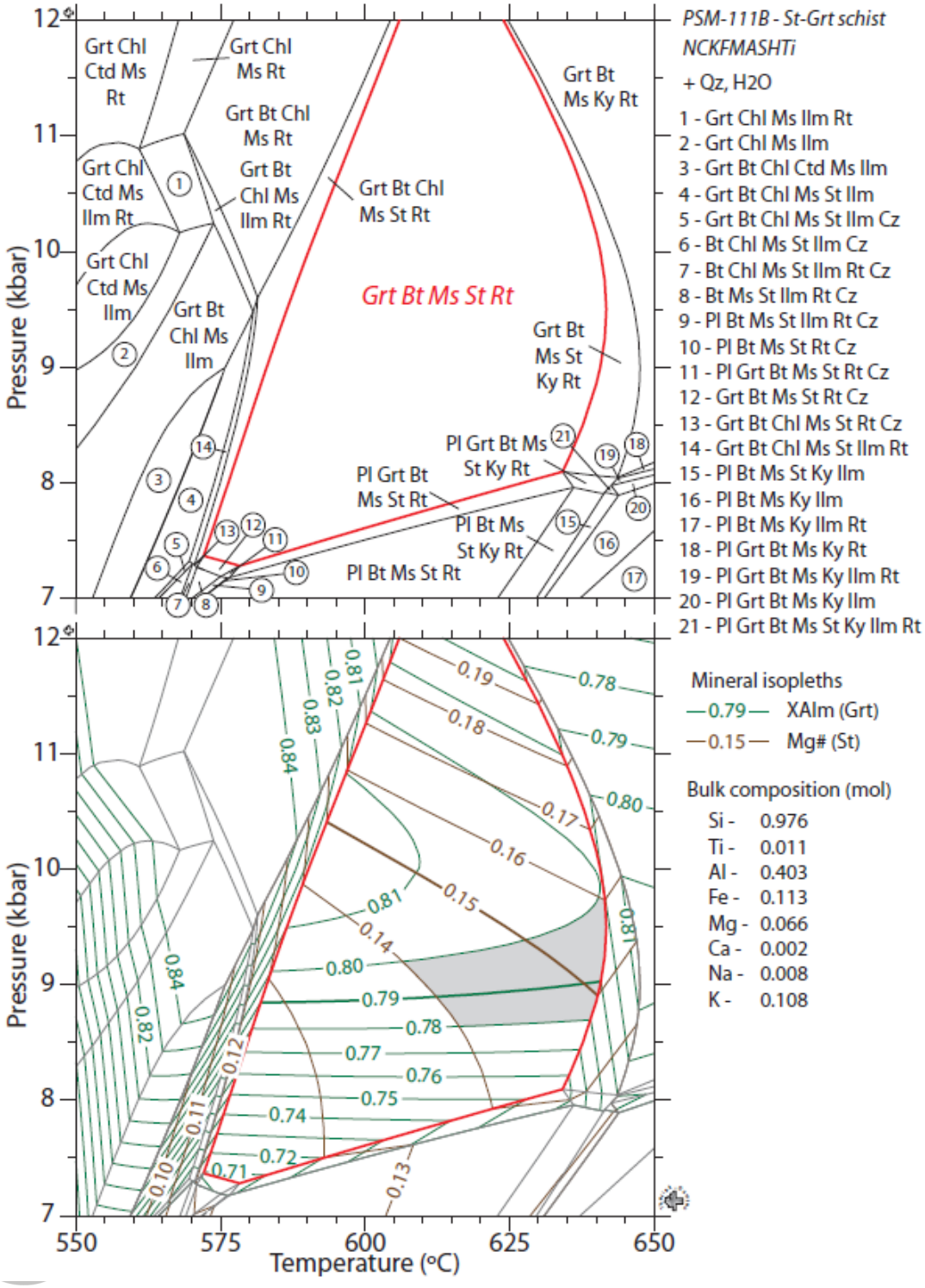

Figure 7. P–T isochemical phase diagram in the NCKFMASHTi system for St-Grt-bearing mica schist (PSM-111B – Embu Complex). All fields are saturated in quartz and water. Top diagram highlights the quadri-variant field for peak assemblage of St+Grt+Ms+Bt+Rt+Qz+H_2O. Bottom diagram shows mineral isopleths for X_{Alm} in garnet (green lines) and Mg# in staurolite (brown lines). Thick lines indicate measured near-peak Mg# of staurolite (0.15±0.01) and X_{Alm} of garnet (0.79±0.01). Estimation of near-peak conditions between 8.5–9.75 kbar and 610–640 °C is shown by a gray polygon. Bulk composition (%wt): SiO_2 (58.64); TiO_2 (0.85); Al_2O_3 (20.54); FeO (8.14); MnO (0.06); MgO (2.66); CaO (0.13); Na_2O (2.26); K_2O (5.11).

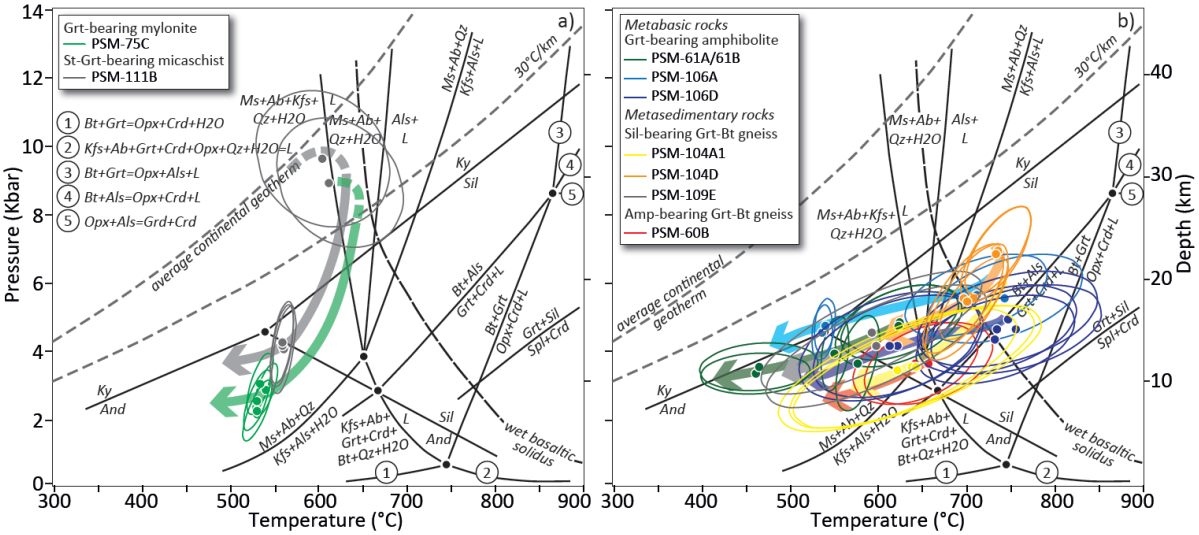

Figure 8. P–T diagrams showing conditions calculated with THERMOCALC and paths for rocks from Embu (a) and Costeiro (b) complexes. For calculations data see Table 1. Ellipse errors are ±1σ. For reference, the grid for the KFMASH system (Spear et al., 1999) and the wet basaltic solidus (Vielzeuf and Schmidt, 2001) is included.

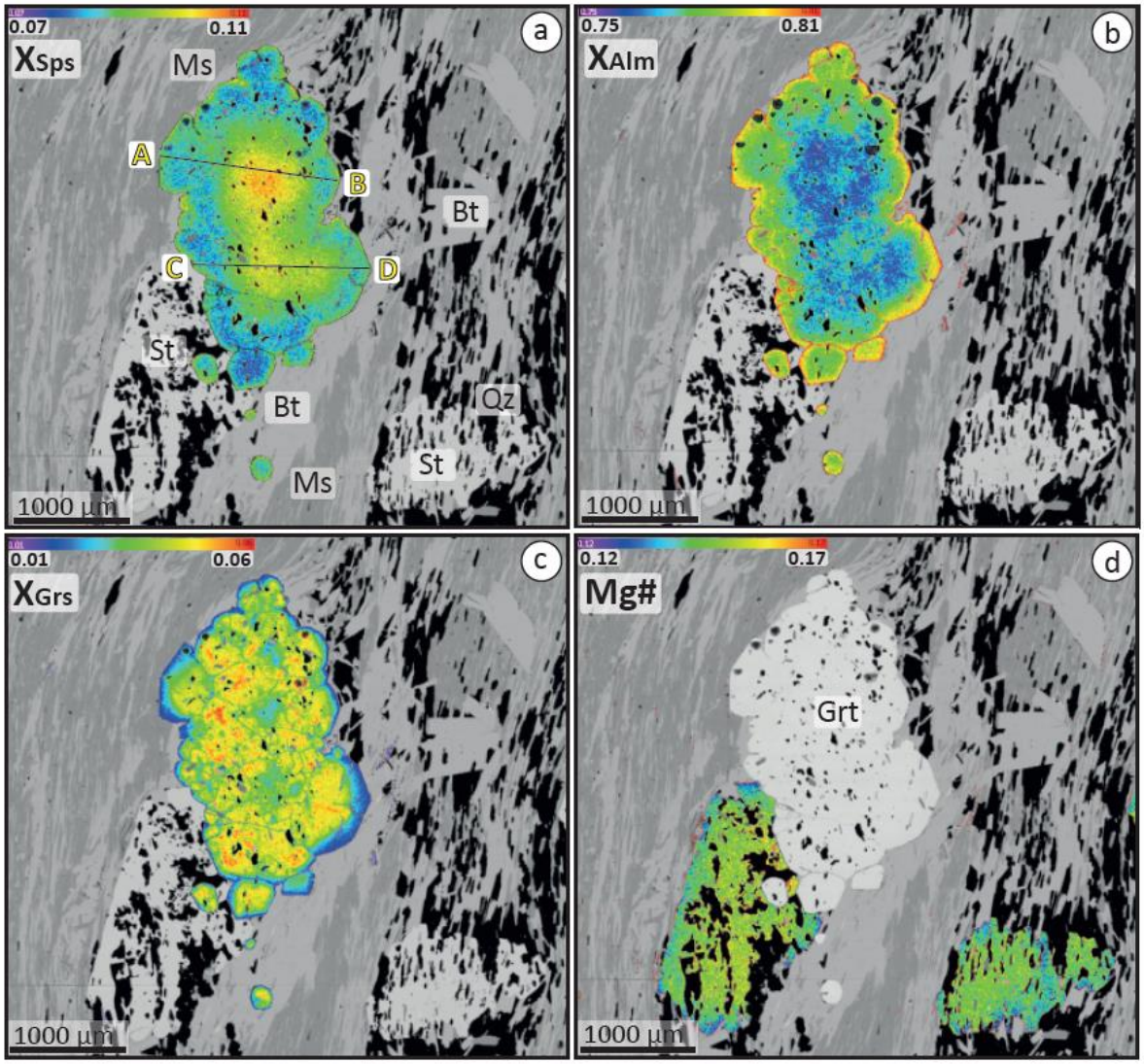

Figure 9. XR images showing key textural and compositional data of the St-Grt-bearing mica schist (PSM-111B – Embu Complex). Color scale bar indicates high (red) and low (blue) concentrations. (a), (b) and (c) X_{Sps} , X_{Alm} and X_{Grs} images of garnet porphyroblast showing normal growing zonation with Mn-rich cores and decreasing in Mn contents towards the rim. The zonation pattern also indicates coalescence of smaller garnet grains. Note that porphyroblasts show a slight increase in Mn and Fe contents and decrease in Ca contents, suggesting retrograde readjustments. The compositional profiles AB and CD are presented in the Supporting Information Figure S1. (d) Mg# image of staurolite porphyroblasts showing re-equilibrated retrograde rims characterized by low Mg# contents. Note that in the contact zone between garnet and staurolite porphyroblasts the retrogression textures are faint or absent.

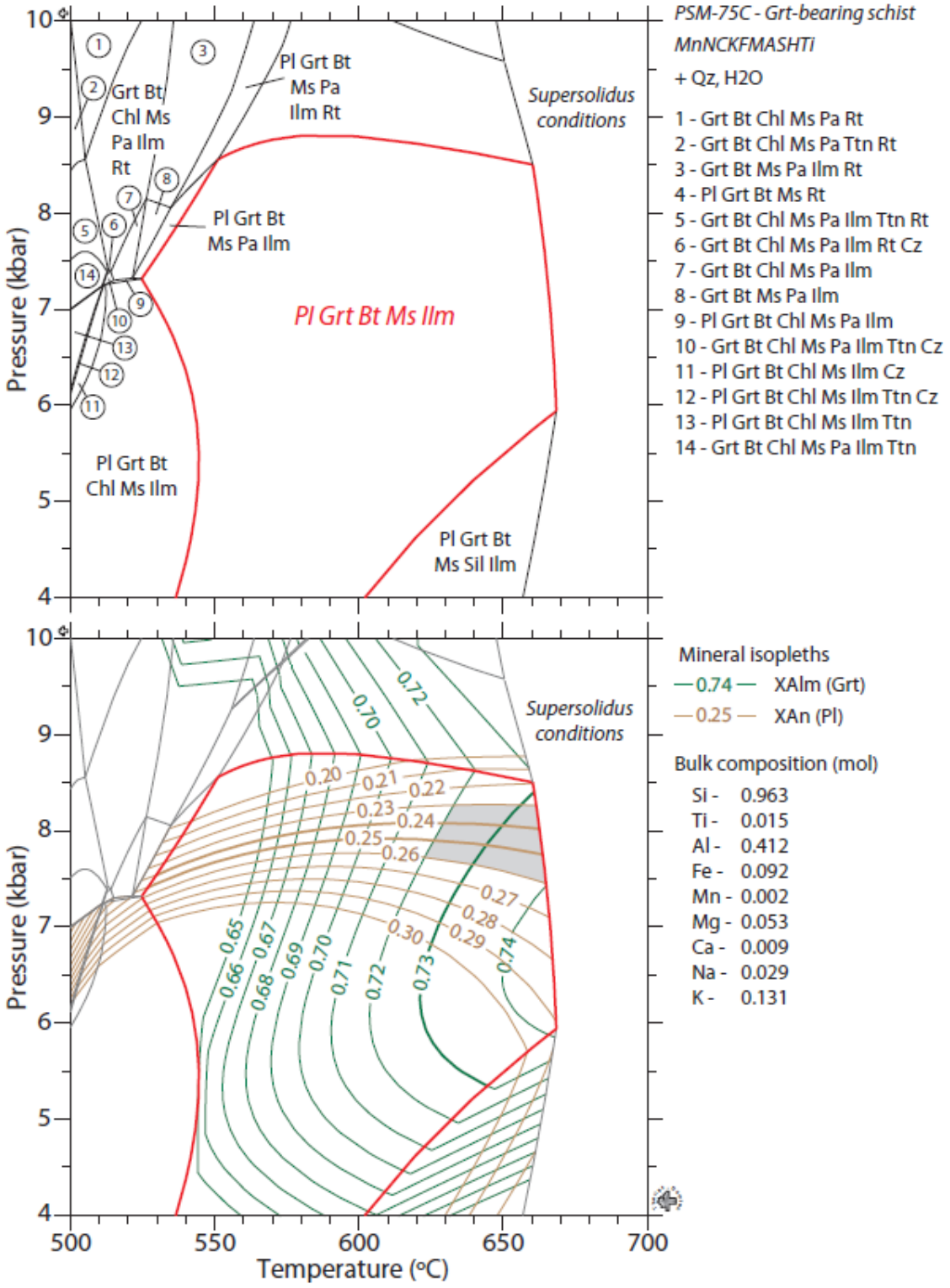

Figure 10. P–T isochemical phase diagram in the MnNCKFMASHTi system for garnet-bearing mica-rich mylonite (PSM-75C – Embu Complex). All subsolidus fields are saturated in quartz and water. Top diagram highlights the penta-variant field for peak assemblage of Grt+Ms+Bt+Pl+Ilm+Qz+H_2O. Bottom diagram shows compositional isopleths of garnet (X_{Alm}) in green and plagioclase (X_{An}) in light brown. Thick lines indicate measured near-peak X_{Alm} of garnet (0.73±0.01) and X_{An} of plagioclase (X_{an}=0.24−0.25±0.01). Estimation of near-peak conditions between 7.4–8.3 kbar and 620–665 °C is shown by a grey polygon. Bulk composition (%wt): SiO_2 (57.85); TiO_2 (1.22); Al_2O_3 (21.00); FeO (6.61); MnO (0.13); MgO (2.15); CaO (0.50); Na_2O (0.89); K_2O (6.19).

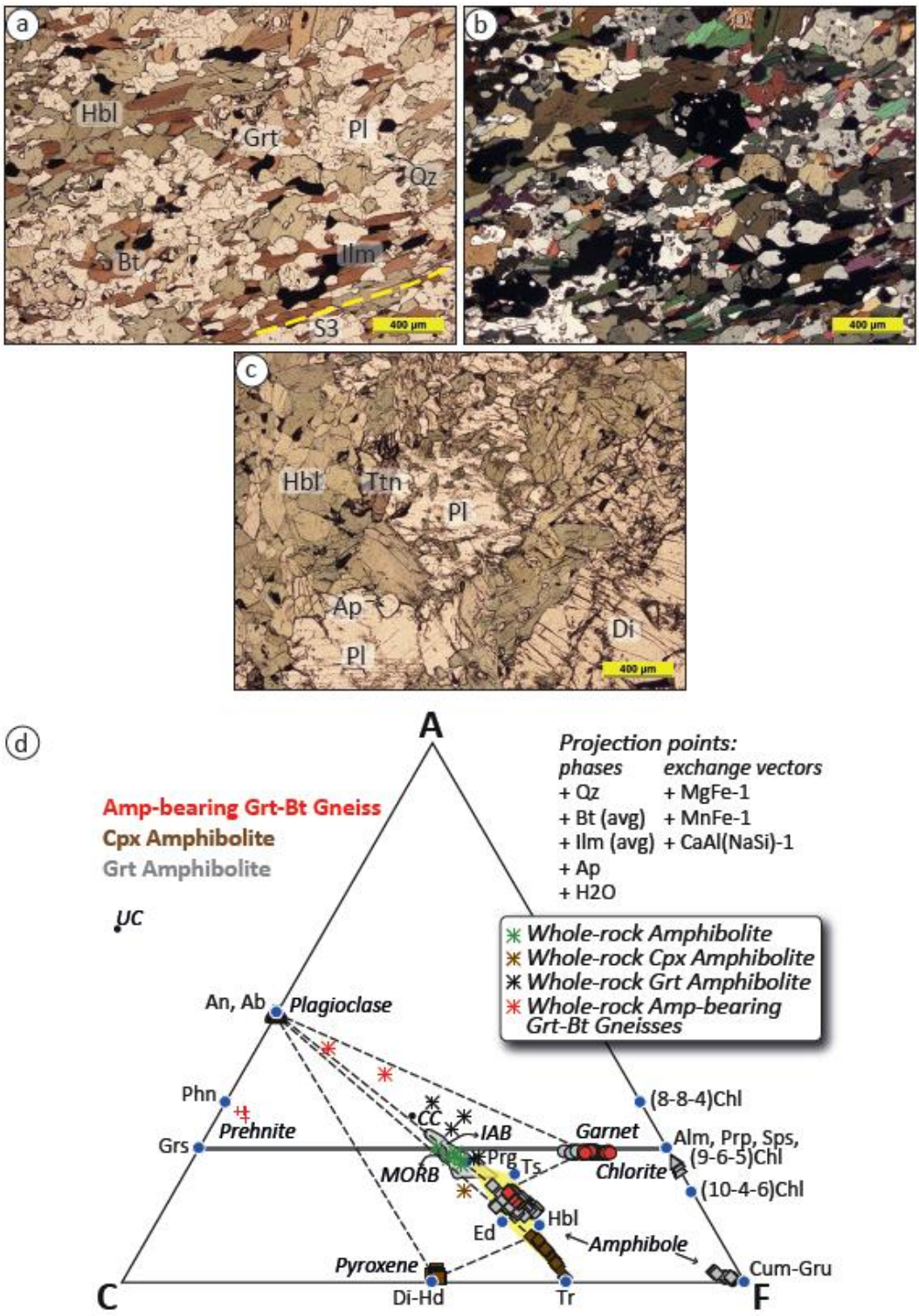

Figure 11. Transmitted light photomicrographs of petrological relationships and ACF compatibility diagram of the amphibolitic rocks from Costeiro Complex. (a) and (b) General texture of medium-grained Grt-Bt-bearing amphibolite (PSM-61B). A common texture of this lithotype comprises rounded quartz inclusions in plagioclase. (c) General texture of coarse-grained Cpx-bearing amphibolite. Images (a) and (c) are in plane-polarized light, and image (b) is in cross-polarized light. (d) ACF compatibility diagram of amphibolitic rocks and amphibole-bearing paragneiss from Costeiro Complex. MORB (mid-ocean ridge basalts) and IAB (island arc basalts) compositions are plotted for comparison.

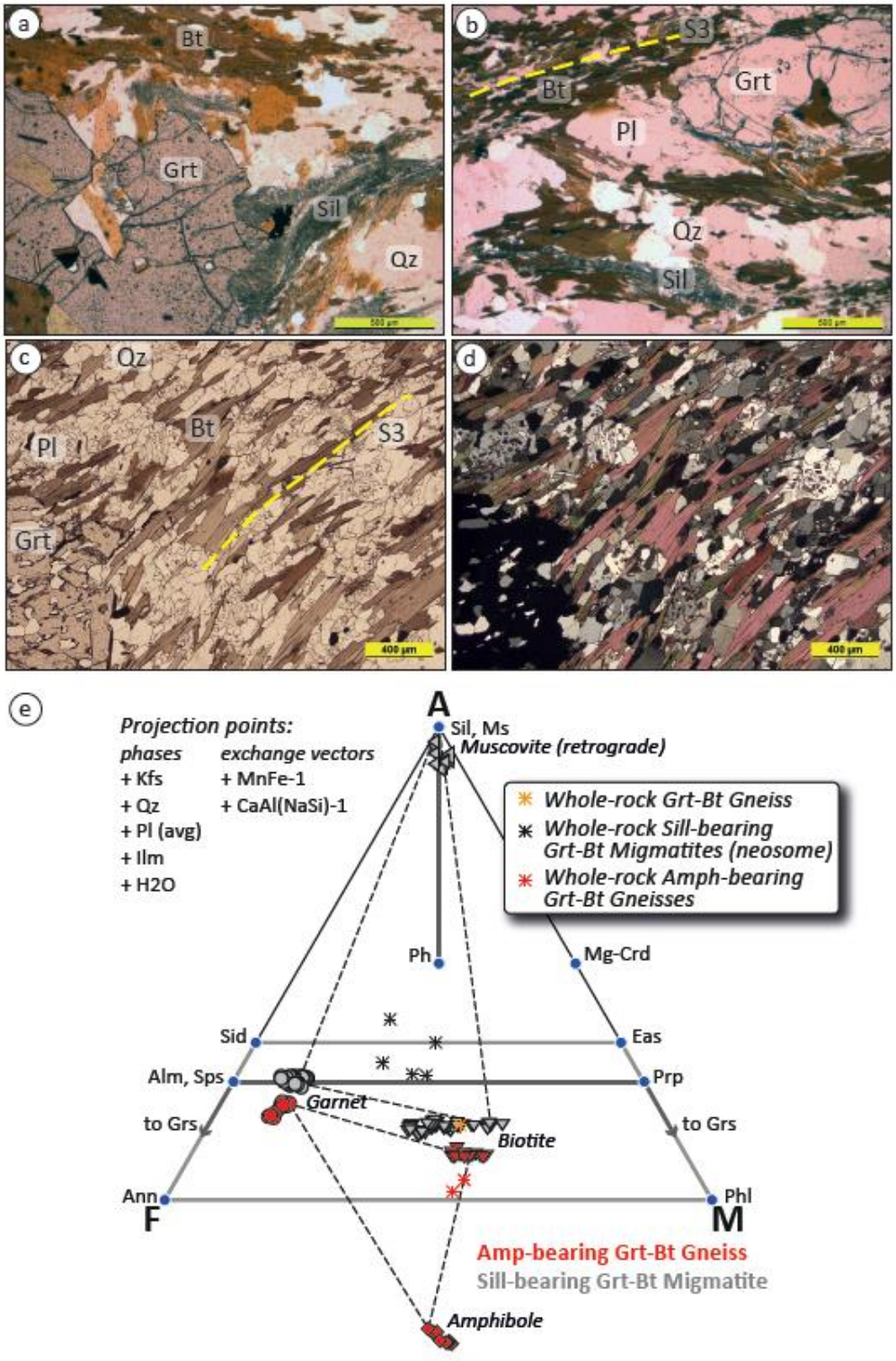

Figure 12. Transmitted light photomicrographs of petrological relationships and AFM compatibility diagram of the metasedimentary rocks from Costeiro Complex. (a) and (b) General texture of porphyroblastic medium- to fine-grained Sil-bearing Grt-Bt migmatitic paragneiss (metapelitic group). (c) and (d) General texture of porphyroblastic medium-grained Amp-bearing Grt-Bt paragneiss (metagreywacke group–PSM-60B). Note the widespread presence of rounded quartz inclusions in plagioclase, similar to those from the Grt-Bt-bearing amphiboles. Images (a), (b) and (c) are in plane-polarized light, and image (d) is in cross-polarized light. (e) AFM compatibility diagram of metasedimentary rocks from Costeiro Complex.

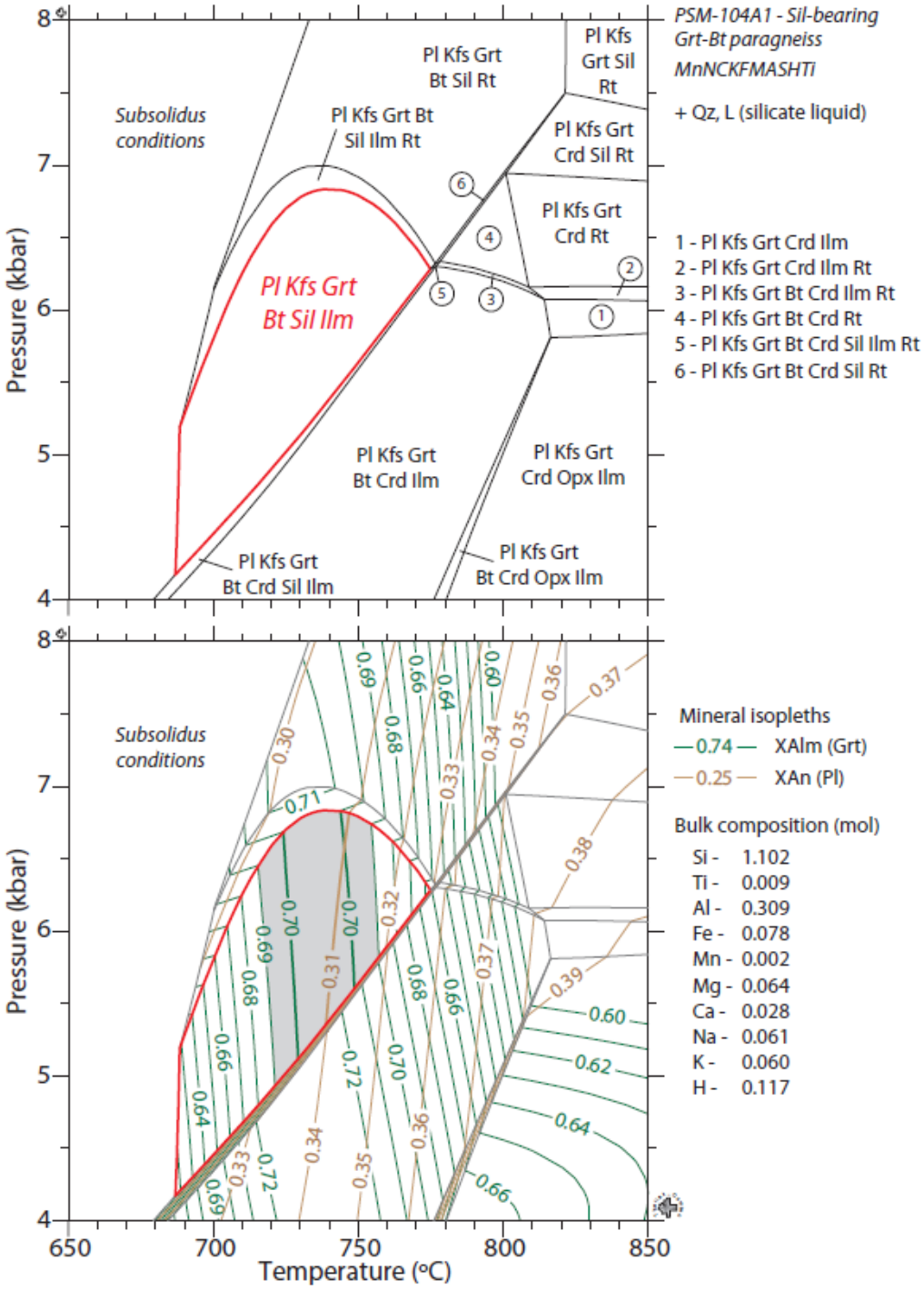

Figure 13. P–T isochemical phase diagram in the MnNCKFMASHTi system for Sil-bearing Grt-Bt paragneiss (PSM-104A1 – Costeiro Complex). All supersolidus fields contain quartz and melt (L=silicate liquid). Top diagram highlights the quadri-variant field for near-peak assemblage of Grt+Sil+Bt+Pl+Kfs+Ilm+Qz+L (L=silicate liquid). Bottom diagram shows compositional isopleths of garnet (X_{Alm}) in green and plagioclase (X_{An}) in light brown. Thick lines indicate measured near-peak X_{Alm} of garnet (0.70±0.01) and X_{An} of plagioclase (0.31±0.01). Estimation of near-peak conditions around 5.0–6.8 kbar and 720–760 °C is shown by a grey polygon. Bulk composition (%wt): SiO_2 (66.23); TiO_2 (0.75); Al_2O_3 (15.75); FeO (5.58); MnO (0.13); MgO (2.58); CaO (1.59); Na_2O (1.89); K_2O (2.82).

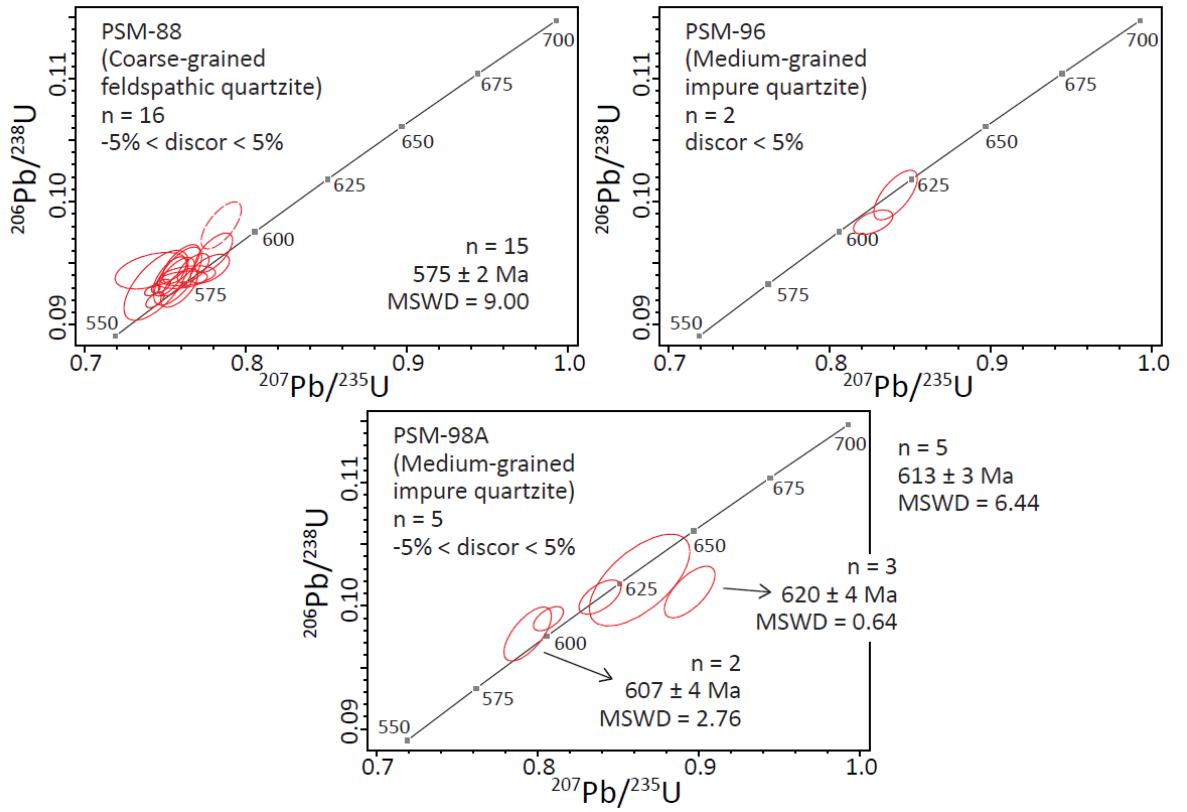

Figure 14. SHRIMP zircon U–Pb data for metamorphic overgrowths on zircon grains of impure quartzites from Embu Complex. Wheterill concordia plots of each sample. Error ellipses are at 95% confidence interval (≈2σ). Dashed ellipses were not used for weighted mean age calculations.

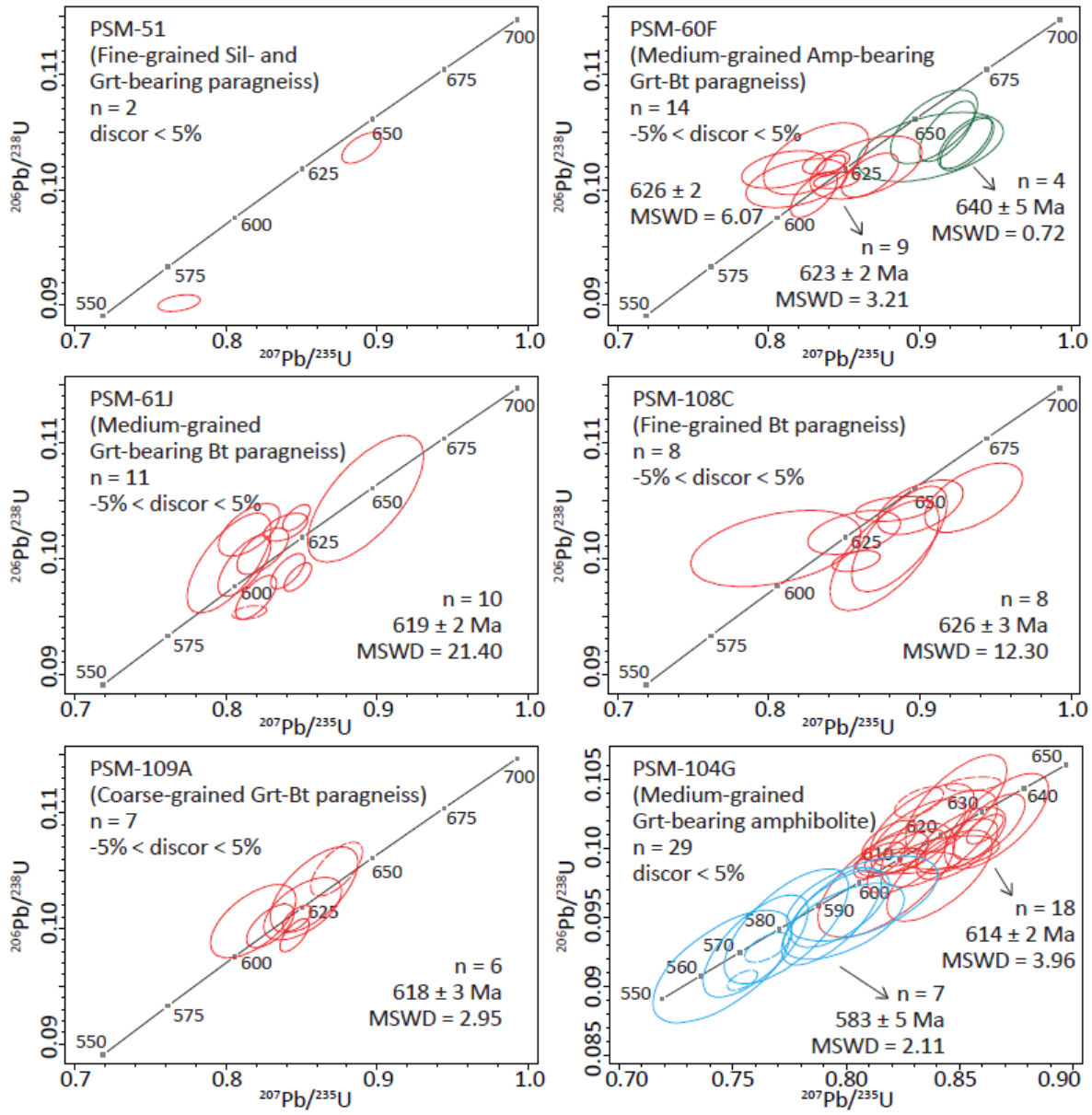

Figure 15. SHRIMP zircon U–Pb data for metamorphic overgrowths on zircon grains of metatexitic paragneisses and garnet-bearing amphibolite of the Costeiro Complex. Wheterill concordia plots of each sample. Error ellipses are at 95% confidence interval (≈2σ). Dashed ellipses were not used for weighted mean age calculations.

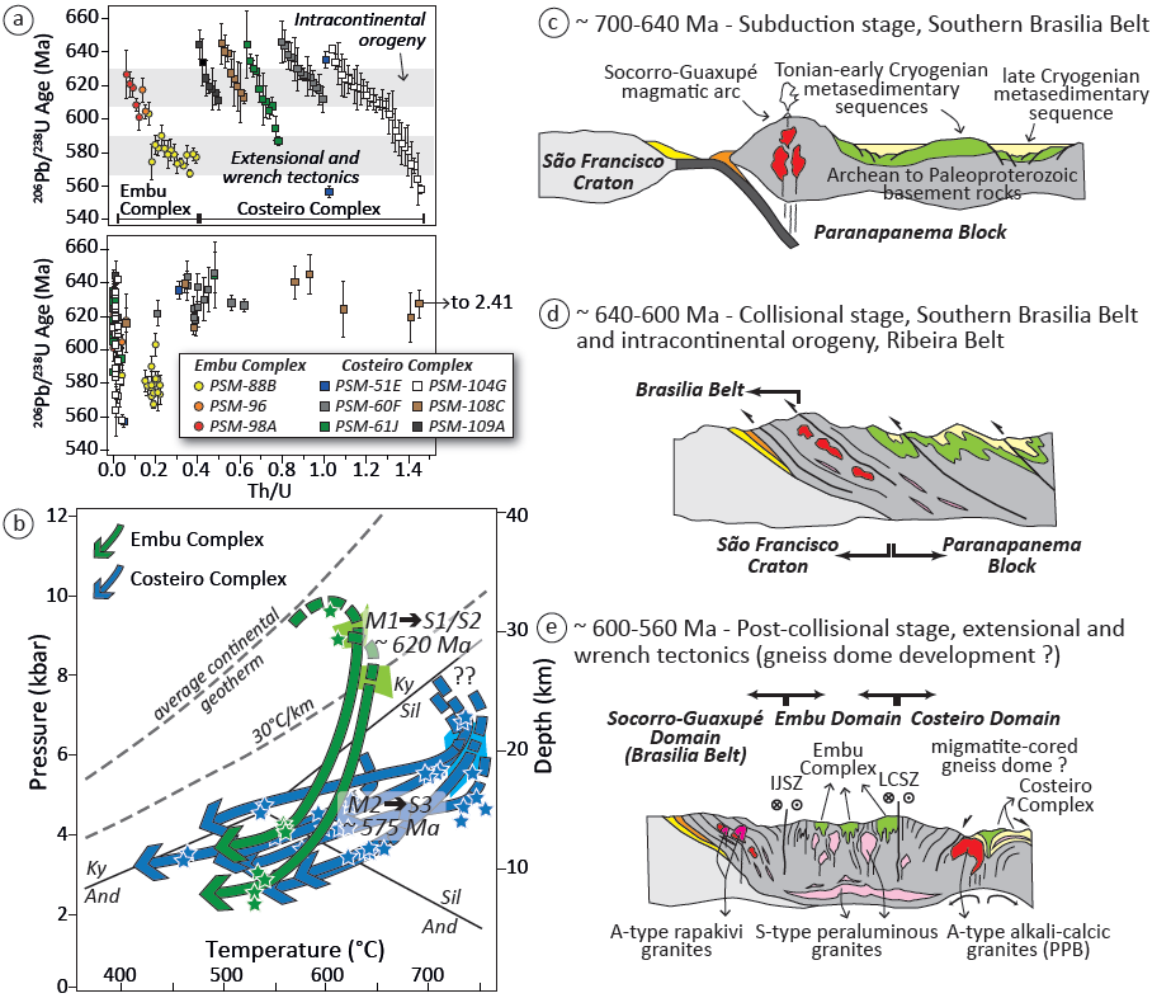

Figure 16. Graphics with data summary and schematic evolutionary model for the late Neoproterozoic tectonic history of the Central Ribeira Belt. The cross-section is not in a geographically straight line (see Meira et al., 2015 for details). (a) Top: $^{206}Pb/^{238}U$ ages with 2σ errors of all metamorphic zircon data from rocks of both Embu and Costeiro complexes, associated with the two tectonic events interpreted to have occurred in the Central Ribeira Belt. See discussion section for explanation. Bottom: $^{206}Pb/^{238}U$ ages *vs.* Th/U plot showing that most of the analyzed zircon overgrowths have low Th/U ratios (lower than 0.25), suggesting a metamorphic origin. The high Th/U ratios of analyses on homogeneous zircon grains and overgrown rims from samples PSM-60F and PSM-108C might be related to the semipelitic (or greywacke) composition of these samples and/or zircon growth or re-equilibration involving a melt phase (Schaltegger et al., 1999). See text for explanation. (b) Integrated P−T–t–d paths for both Embu and Costeiro complexes. Light green and light blue fields indicate P−T estimations from isochemical phase diagrams for Embu and Costeiro domains, respectively. Green and blue stars indicate P−T data from optimal thermobarometry for Embu and Costeiro domains, respectively. Abbreviations: M1, first metamorphism; M2, second metamorphism; S1, S1 foliation; S2, S2 foliation; S3, S3 foliation; (c) Subduction stage of Southern Brasilia Belt at circa 700–640 Ma (e.g. Campos Neto et al., 2000; Trouw et al., 2000; Rocha et al., 2018; Tedeschi et al., 2018). (d) Collisional stage in Southern Brasilia Belt (e.g. Campos Neto et al., 2011; Reno et al., 2012; Tedeschi et al., 2017, 2018; Rocha et al., 2018) and intracontinental orogeny in Central Ribeira Belt at around 640–600 Ma. (e) Post-collisional stage at circa 600–560 Ma, characterized by voluminous S-type peraluminous magmatism and wrench tectonics in the Embu Domain, and calc-alkaline/alkali-calcic magmatism, widespread migmatization and gneiss domes development in the Costeiro Domain. Note the intrusion of A-type rapakivi granite and associated high-K calc-alkaline granitoids in the Socorro-Guaxupé Domain (see Janasi et al., 2009). Abbreviations: IJSZ, Itu-Jundiuvira Shear Zone; LCSZ, Lancinha-Cubatão Shear Zone.